

# 1 Projection-specific integration of convergent 2 thalamic and retrosplenial signals in the 3 presubicular head direction cortex

## 4 5 Authors

6 Louis Richevaux<sup>1\*</sup>, Dongkyun Lim<sup>1</sup>, Mérie Nassar<sup>1</sup>, Léa Dias Rodrigues<sup>1</sup>, Constanze Mauthe<sup>1</sup>,  
7 Ivan Cohen<sup>3</sup>, Nathalie Sol-Foulon<sup>2</sup>, Desdemona Fricker<sup>1,4\*</sup>

8 <sup>1</sup>Université Paris Cité, CNRS, Integrative Neuroscience and Cognition Center, F-75006 Paris,  
9 France, <sup>2</sup>Sorbonne Université, INSERM, CNRS, Paris Brain Institute, ICM, Pitié-Salpêtrière  
10 Hospital, F-75013 Paris, France, <sup>3</sup>Sorbonne Université, INSERM, CNRS, Neuroscience Paris  
11 Seine, Institut de Biologie Paris Seine, F-75005 Paris, France, <sup>4</sup>Lead contact.

12 Correspondence: [desdemona.fricker@parisdescartes.fr](mailto:desdemona.fricker@parisdescartes.fr), [louis.richevaux@parisdescartes.fr](mailto:louis.richevaux@parisdescartes.fr)

## 13 14 Summary

15 Head-direction (HD) signals function as the brain's internal compass. They are  
16 organized as an attractor, and anchor to the environment via visual landmarks. Here we  
17 examine how thalamic HD signals and visual landmark information from the retrosplenial  
18 cortex combine in the presubiculum. We find that monosynaptic excitatory connections  
19 from anterior thalamic nucleus and from retrosplenial cortex converge on single layer 3  
20 pyramidal neurons in the dorsal portion of mouse presubiculum. Independent dual  
21 wavelength photostimulation of these inputs in slices leads to action potential generation  
22 preferentially for near-coincident inputs, indicating that layer 3 neurons can transmit a  
23 visually matched HD signal to medial entorhinal cortex. Layer 4 neurons, which innervate the  
24 lateral mammillary nucleus, form a second step in the association of HD and landmark  
25 signals. They receive little direct input from thalamic and retrosplenial axons. We show that  
26 layer 4 cells are excited di-synaptically, transforming regular spiking activity into bursts of  
27 action potentials, and that their firing is enhanced by cholinergic agonists. Thus, a coherent  
28 sense of orientation involves projection specific translaminar processing in the  
29 presubiculum, where neuromodulation facilitates landmark updating of HD signals in the  
30 lateral mammillary nucleus.

31

32

## 33 Keywords

34 Keywords: postsubiculum, presubiculum, head direction, multisensory, dendritic integration,  
35 circuit mechanism, patch clamp, brain slices, layer specific, projection specific

36

37

## 38 Introduction

39 The head direction (HD) system functions as the brain's compass system. It is  
40 distributed across several interconnected brain structures, and hierarchically organized from  
41 the brainstem to the lateral mammillary nucleus (LMN; Stackman and Taube, 1998), the  
42 anterior thalamic nuclei (ATN; Taube, 1995), and the dorsal Presubiculum (PrS; Ranck, 1984;  
43 Taube et al., 1990a). Modeling work suggests the HD system functions as a ring attractor,  
44 where the population of HD neurons is arranged in a one dimensional manifold (Blair and  
45 Sharp, 1995; McNaughton et al., 2006; Skaggs et al., 1995). The activity of thalamic and PrS  
46 HD neurons is correlated across different brain states, even during sleep, independently of  
47 sensory cues (Peyrache et al., 2015). The bump-like activity dynamics of an attractor  
48 network can maintain HD signals based on excitatory-excitatory or excitatory-inhibitory  
49 interactions (Knierim and Zhang, 2012; Simonnet et al., 2017). However, HD signals may drift  
50 in the dark (Taube et al., 1990b; Zugaro et al., 2003). For precise navigation, internally  
51 generated information on head direction must be combined with awareness of location in an  
52 environment. Mechanisms underlying the combination of egocentric head direction signals  
53 with anchoring to allocentric landmarks remain to be clarified.

54  
55 Head direction and visual landmark signals may be integrated in the presubiculum  
56 (Jeffery et al., 2016; Yoder et al., 2019). Head direction cells are found in the superficial and  
57 deep layers of dorsal presubiculum, also termed postsubiculum (Boccaro et al., 2010), and  
58 most layer 3 neurons in the dorsal presubiculum are head direction cells (Tukker et al., 2015;  
59 Preston-Ferrer et al., 2016). These cells receive monosynaptic head direction inputs from the  
60 anterior thalamus (Nassar et al., 2018; Peyrache et al., 2015; Balsamo et al., 2022). Lesions  
61 of the PrS impair the visual landmark control of a cell's preferred direction in ATN and in  
62 LMN (Goodridge and Taube, 1997; Yoder et al., 2015). Presubicular lesions also induce place  
63 field instability in the hippocampus (Calton et al., 2003), suggesting this region may be  
64 crucial to the anchoring of directionally modulated neurons to environmental landmarks.

65  
66 Landmark based navigation depends on reliable visual cues. The PrS appears to  
67 receive direct projections from the primary visual cortex and indirect visual input via the  
68 retrosplenial cortex (Van Groen & Wyss 2003; Vogt & Miller 1983). The retrosplenial cortex  
69 encodes angular head velocity (Alexander & Nitz 2015; Keshavarzi et al. 2022) and visual  
70 landmark information (Auger et al., 2012; Clark et al., 2010; Sit and Goard, 2023). In  
71 particular, neurons in the dysgranular retrosplenial cortex encode landmark-dominated  
72 head-direction signals (Jacob et al., 2017). Presubicular layer 3 cells receiving projections  
73 from both the anterior thalamus and the retrosplenial cortex (Kononenko and Witter 2012)  
74 could update the compass and bind landmarks to head direction signals. Presubicular  
75 neurons could then broadcast integrated HD-landmark signals directly to the MEC, via deep  
76 layers to the ADN and via layer 4 neurons to the LMN (Huang et al., 2017; Yoder et al., 2015;  
77 Yoder and Taube, 2011). The different target-specific presubicular projection neurons are  
78 well positioned to integrate anterior thalamic and retrosplenial inputs, but technical  
79 constraints have limited understanding of how known anatomical inputs are transformed  
80 into functional integrated output signals.

81

82 This work was therefore designed to examine integration of visual landmarks and head  
83 direction signals in the PrS. Retrograde tracing was used to confirm inputs to the PrS from  
84 the ATN and the RSC. The spatial distribution of ATN and RSC targets in the dorsal and  
85 ventral PrS was investigated by stereotaxic injection of viral vectors inducing anterograde  
86 expression of light-gated ion channels fused to fluorescent reporters. We found that  
87 superficial layers of the dorsal PrS are major targets of ATN and RSC projections. We  
88 analyzed functional convergence of these inputs in the PrS using dual-wavelength  
89 optogenetic stimulations in ex vivo brain slices, while recording from layer 3 and 4 pyramidal  
90 neurons. Both ATN and RSC projections made mono-synaptic excitatory connections with  
91 single layer 3 principal cells and mostly di-synaptic ones with layer 4 cells. We show that  
92 EPSPs induced with close to coincident timing by ATN and RSC fibers summed non-linearly in  
93 layer 3 neurons. Layer 4 cell firing is facilitated by cholinergic activation. These data provide  
94 insights into the integration of landmark and head direction inputs and their distribution to  
95 downstream targets by PrS pyramidal cells.

96

## 97 **Results**

### 98 **ATN and RSC send strong axonal projections to the dorsal Presubiculum**

99 The origins of the main afferents projecting to the presubiculum were explored by  
100 injecting retrogradely transported fluorescent beads into the PrS (Figure 1A). After 4 days,  
101 coronal slices were prepared to examine the injection site and transport of the beads. Some  
102 beads remained close to the PrS injection site, due in part to local projections. Strong bead  
103 signals were detected within the two subnuclei that form the anterior thalamus, the  
104 anterodorsal (AD) and anteroventral (AV) part of ATN. Neurons in AD were labeled most  
105 strongly in the medial portion of the AD, while labeled neurons in AV were found in its  
106 lateral portion (Figure 1B). Many neurons in the RSC were labeled. Cells with somata in  
107 layers 2 and 5 of the dysgranular dRSC were labeled, while mostly layer 5 cells of granular  
108 gRSC contained beads (Figure 1C). Regions adjacent to the presubiculum including the  
109 subiculum (Sub), parasubiculum (PaS) and the medial and lateral entorhinal cortices (MEC,  
110 LEC) were labeled as was the contralateral PrS. Beads were also detected in the laterodorsal  
111 thalamic nucleus (LD). Figure 1—figure supplement 1 shows an example of a series of  
112 labeled coronal sections, indicating some labeling also in the visual cortices, perirhinal  
113 cortex, the nucleus reuniens of the thalamus, the dorsolateral geniculate nucleus, and the  
114 claustrum. Some beads were observed in the CA1 region, which has not previously been  
115 reported. Potentially though, this labeling could derive from a bead leak into the nearby PaS  
116 which is innervated by CA1 (Van Groen et Wyss 1990a). In summary, the ATN and RSC are  
117 the major sources of afferents projecting to the presubiculum with lesser inputs from other  
118 sites.

119 Projections from the ATN or RSC to the presubiculum were explored by injecting at  
120 these sites an anterogradely transported viral construct which expressed the modified  
121 Channelrhodopsin Chronos fused to GFP (Figure 1D). After 4 weeks, horizontal slices were  
122 prepared to verify the ATN injection site. Chronos-GFP labeling was mostly confined to the  
123 ATN, occasionally extending to medial thalamic and reticular nuclei nearby, possibly as  
124 bundles of projecting fibers (Figure 1E). After injection at the RSC site, coronal sections  
125 (Figure 2F) showed strong expression in layer 5, especially deeper zones, and layer 6 of both  
126 dysgranular and granular RSC, while labeled dendrites were evident in layer 1. Chronos-GFP  
127 expression extended throughout the RSC, from -1.7 to -3.7 posterior to Bregma on the

128 antero-posterior axis.

129 Projections of the ATN to the presubiculum were examined in horizontal sections  
130 (Figure 1G). ATN axons expressing the Chronos-GFP construct targeted layers 1 and 3 of the  
131 presubiculum, avoiding layer 2 (Simonnet et al., 2017; Nassar et al., 2018). Labeling was  
132 precisely limited to the presubiculum with a sharp reduction of green fluorescence at the  
133 posterior border with the parasubiculum, the anterior border with the subiculum and the  
134 lateral border with deep layers. Axon terminals in layer 3 were not homogeneously  
135 distributed. Patches of higher density were evident in deep layer 3 (Figure 1G). Along the  
136 dorso-ventral axis, ATN axons projected from -2 to -4 mm ventral to Bregma. Fluorescence  
137 was not detected in adjacent regions including the Sub, PaS, and DG. ATN axons avoided  
138 layer 2 of the PrS, including anterior regions with patches of calbindin positive neurons that  
139 project to contralateral PrS (Preston-Ferrer et al. 2016; Figure 1K).

140 RSC projections to the presubiculum (Figure 1H), traced with the fluorescent  
141 Chronos-GFP construct, also projected to layers 1 and 3. Unlike ATN axons, they were  
142 restricted to dorsal regions of the presubiculum (from -2 to -3 mm ventrally to Bregma on  
143 the dorso-ventral axis; Figure 1H, I, J). RSC axon labeling tended to avoid patches of high-  
144 density ATN projections (Figure 1G, K. Figure 3). Overall, these data show ATN and RSC  
145 afferents innervate overlapping dorsal regions of the PrS, in layer 1 and deep parts of layer 3.  
146 Different spatial patterns of fiber terminations suggest distinct local connectivities.

147

### 148 **Layer 3 neurons are directly excited by both ATN and RSC afferents**

149 We next examined physiological effects of ATN and RSC afferents on PrS pyramidal  
150 cells (Rees et al., 2017). Responses to photo-stimulation of the Chronos-GFP construct  
151 injected either in the thalamus or in the retrosplenial cortex (Figure 2A) were recorded in  
152 layer 3 neurons (Figure 2B). These cells had robust regular firing patterns in response to  
153 depolarizing current injections (Figure 2C). Intrinsic properties of layer 3 cells were rather  
154 uniform (Figure 2—figure supplement 1) and an unsupervised cluster analysis suggested  
155 they formed a single population (Figure 2D).

156 Blue light activation of either ATN or RSC axons expressing Chronos-GFP reliably  
157 evoked synaptic responses in whole-cell patch-clamp records from layer 3 cells. High  
158 intensity stimulation (1 - 3 mW) evoked EPSCs or EPSPs with a probability of 84% (70/83) for  
159 ATN fibers and 85% (104/123) for RSC fibers (Figure 2E). Excitatory postsynaptic currents or  
160 potentials evoked by optical stimulation of thalamic and retrosplenial inputs will be referred  
161 to as oEPSCs and oEPSPs. Mean oEPSC amplitudes (Figure 2F) were similar for ATN ( $-305.0 \pm$   
162  $61.0$  pA,  $n = 24$ ) and RSC fiber stimuli ( $-305.8 \pm 59.1$  pA,  $n = 27$ ). Response latency (Figure  
163 2G) to ATN axon stimulation was  $2.45 \pm 0.19$  ms ( $n = 24$ ) and that for RSC axon stimulation  
164 was  $2.93 \pm 0.23$  ms ( $n = 27$ ). The variability in latency of oEPSCs (Figure 2—figure  
165 supplement 2A, B) induced by RSC afferent stimuli was  $0.35 \pm 0.09$  ms ( $n = 27$ ) and that for  
166 oEPSCs induced by ATN stimuli was  $0.19 \pm 0.06$  ms ( $n = 24$ ). These short oEPSC latencies  
167 suggest monosynaptic transmission. We confirmed this point by showing that oEPSCs were  
168 maintained in presence of TTX ( $1\mu\text{M}$ ) and 4AP ( $100\mu\text{M}$ ) (Figure 2H,  $n = 2$  and  $12$  for ATN and  
169 RSC respectively). EPSCs induced by stimulation of ATN and RSC fibers were reduced in  
170 amplitude and decayed more quickly in the presence of the NMDA receptor antagonist APV  
171 ( $50 \mu\text{M}$ ) and were completely abolished by further application of the AMPA receptor  
172 antagonist NBQX ( $1 \text{ mM}$ ) (Figure 2I). The shape of oEPSCs induced by light stimulation of  
173 ATN and RSC fibers was comparable. Rise times were  $1.38 \pm 0.15$  ms for ATN EPSCs ( $n = 15$ )  
174 and  $1.38 \pm 0.08$  ms for RSC-mediated EPSCs ( $n = 15$ ) and mean half-widths were  $4.00 \pm 1.02$



175 ms for ATN-induced EPSCs ( $n = 15$ ) and  $4.34 \pm 1.18$  ms for RSC EPSCs ( $n = 15$ ). The mean time  
176 constant (tau decay) for ATN-mediated EPSCs was  $3.01 \pm 0.21$  ( $n = 15$ ) and for RSC-induced  
177 EPSCs  $3.17 \pm 0.27$  ( $n = 15$ ) (Figure 2—figure supplement 2C-E.).

178 Optical stimulation of ATN and RSC fibers at lower light intensities elicited sub-  
179 threshold synaptic events in layer 3 cells. oEPSP amplitude for ATN mediated events was  
180  $4.09 \pm 1.18$  mV ( $n = 11$ ) and for RSC events it was  $4.80 \pm 0.84$  mV ( $n = 11$ ). Maximal rising  
181 slopes were  $2.93 \pm 0.82$  mV/ms for ATN-mediated events ( $n = 11$ ) and  $3.02 \pm 0.53$  mV/ms for  
182 RSC EPSPs ( $n = 11$ ), and decay time constants were  $81.4 \pm 11.6$  ms for ATN EPSPs ( $n = 11$ ) and  
183  $86.9 \pm 11.2$  ms for RSC EPSPs ( $n = 11$ ). Rise times were shorter for subthreshold EPSPs  
184 induced by ATN afferents at  $3.00 \pm 0.24$  ms ( $n = 11$ ) while those for RSC initiated EPSPs were  
185  $3.59 \pm 0.34$  ( $n = 11$ ,  $p = 0.042$ , Wilcoxon test; Figure 2—figure supplement 2F-J). These data  
186 show that ATN and RSC axons make monosynaptic, glutamatergic excitatory contacts on  
187 layer 3 PrS cells.

188 The dynamics of responses to repetitive stimulation of layer 3 PrS cells were tested  
189 using 20 Hz trains of light stimuli to activate either ATN or RSC afferents. oEPSCs for both  
190 inputs followed depressing kinetics. Amplitude decreased for both inputs (Figure 2J, K),  
191 significantly after the fourth pulse (Friedman's test and Dunn's multiple comparison test).  
192 The  $10/1$  ratio was significantly lower than the paired-pulse ratio (PPR) in both cases (ATN  
193  $10/1$   $0.56 \pm 0.05$  vs PPR  $0.86 \pm 0.05$ ,  $n = 15$ ,  $p < 0.0001$ , Wilcoxon test, RSC  $10/1$   $0.64 \pm 0.05$   
194 vs PPR  $0.83 \pm 0.03$ ,  $n = 15$ , Wilcoxon test) (Fig 2L). ATN fiber stimulation induced PrS cell  
195 firing in current-clamp with a high probability for initial stimuli and lower stable probabilities  
196 for later stimuli in the train. Similarly, 20 Hz stimulation of RSC afferents evoked spikes with  
197 high probability for initial stimuli and decreasing probabilities for later stimuli (on fourth and  
198 7<sup>th</sup>-10<sup>th</sup> pulses, Friedman's and Dunn's multiple comparison tests; Figure 2M, N). Responses  
199 to repeated subthreshold stimuli had similar dynamics (Figure 2O). Stimulation with lower  
200 light intensities ( $< 1$  mW) to initiate sub-threshold oEPSPs elicited different dynamic  
201 responses. ATN afferent trains elicited responses with depressing dynamics: the amplitude  
202 of the fifth oEPSP was significantly less than the first one ( $3.18 \pm 0.88$  vs  $5.11 \pm 1.64$  mV,  $p =$   
203  $0.0185$ , Friedman's and Dunn's tests). In contrast, subthreshold 20 Hz stimulation of RSC  
204 afferents evoked little or no oEPSP depression (Figure 2—figure supplement 2K-M). These  
205 data reveal distinct patterns of integration of repetitive activity in glutamatergic ATN and RSC  
206 afferents terminating on PrS layer 3 pyramidal cells.

207

### 208 **Convergence of ATN and RSC inputs on single layer 3 neurons**

209 Are single layer 3 pyramidal cells innervated by both ATN and RSC afferents? It  
210 seemed likely since the probability of connection to a given cell was 84% for ATN fibers and  
211 85% for RSC afferents, and cluster analysis (Figure 2D) provided no evidence for  
212 subpopulations of layer 3 cells (but see Balsamo et al., 2022).

213 We tested the hypothesis using photostimulation at two different light frequencies to  
214 activate ATN and RSC afferents independently. However this approach may be compromised  
215 since there is an overlap in the excitation spectra of blue-light activated Chronos (400-600  
216 nm) and red-light activated Chrimson (450-700 nm; Klapoetke et al., 2014). Excitation of  
217 Chronos with high intensities of blue light might also excite Chrimson. Stimulating with red  
218 light at 630 nm should elicit neurotransmitter release in Chrimson-containing but not  
219 Chronos-expressing fibers, which we found was indeed the case. Blue light stimuli at 470 nm  
220 and intensities higher than 0.01 mW elicited oEPSPs in layer 3 cells of animals with Chronos-  
221 expressing fibers. In contrast, blue light intensities higher than 0.25 mW were needed to

222 induce oEPSPs in different animals with Chrimson-expressing axons (Figure 3—figure  
223 supplement 1A-D). Moreover, the amplitude of these events was smaller in Chrimson-  
224 injected than in Chronos-injected mice. Thus, in our experimental conditions, blue light  
225 intensities up to 0.25 mW could be used to excite Chronos-positive axons with confidence  
226 that Chrimson-expressing fibers would not be stimulated.

227 We also tested the inverse, red light component of the dual stimulus strategy.  
228 Intensities were tested in mice injected either with AAV5-Chronos to label ATN fibers or  
229 AAV5-Chrimson to label RSC afferents. The strategy was validated by showing that red light  
230 induced oEPSPs in Chrimson-containing, but not Chronos-expressing fibers, while blue light  
231 evoked synaptic events in Chronos-, but not Chrimson-expressing fibers (Figure 3—figure  
232 supplement 1E-K).

233 Injection in the same animal of the Chronos construction to the thalamus and that  
234 for Chrimson to the retrosplenial cortex let us visualize ATN and RSC afferents to the  
235 presubiculum (Figure 3A, B). Axon terminal fields of ATN and RSC projections were evident in  
236 superficial layers of dorsal PrS (cf. Figure 1). Layer specificities, and labeling inhomogeneities  
237 were apparent as were high density ATN patches below layer 2 with no RSC axon innervation  
238 (Figure 3B). Layer 3 pyramidal cells could be innervated by ATN and RSC contacts both with  
239 apical dendrites in layer 1 and basilar dendrites of layer 3 (Figure 3D). We found optical  
240 stimulation of ATN and RSC axons, evoked synaptic responses in 14 out of 17 layer 3  
241 pyramidal cells tested (current-clamp and voltage-clamp; Figure 3E, F).

242 In order to quantify substrates of these innervations, we counted numbers of labeled  
243 ATN or RSC terminals located at less than  $1\mu\text{m}$  from dendrites of biocytin filled layer 3  
244 pyramidal cells ( $n = 6$ ; Figure 3G). The distribution of these potential contact sites on  
245 dendritic trees of layer 3 neurons was diverse. Some neurons exhibited highly segregated  
246 domains receiving either ATN or RSC inputs. For instance, cell 1 had a high proportion of  
247 clustered RSC putative synapses on its apical tuft while basilar dendrites were mostly  
248 surrounded by potential thalamic terminals. In cell 2, RSC terminals were clustered close to  
249 apical dendrites and also together with ATN terminals close to basilar dendrites. In contrast,  
250 many ATN terminals were located closer to apical dendrites of cell 3. Segregation of cortical  
251 RSC inputs to apical dendrites and thalamic ATN inputs to basal dendrites might favor  
252 supralinear EPSP summation. However, afferent terminal distributions differed and we found  
253 no clear pattern of sub- or supralinear summation (cell 1, supralinear summation  
254 (Dual/summed EPSP, 1.39); cell 2, roughly linear (0.91); cell 3, sublinear (0.69), Figure 3G, H).  
255 Furthermore, we noted certain potential contacts were located with separations less than 20  
256  $\mu\text{m}$  on the same dendrite (Figure 3I). Such proximity might underly local dendritic  
257 computations and supra-linearities such as NMDA-mediated dendritic spikes which are  
258 suggested to contribute to non-linear summation of synaptic events (Larkum et al., 1999,  
259 2007, 2009).

260

### 261 **Supralinear integration and amplification of ATN and RSC excitatory postsynaptic** 262 **potentials**

263 We explored interactions between excitatory inputs to layer 3 neurons by stimulating  
264 ATN and RSC axons separately with blue or red light. Excitatory synaptic potentials evoked by  
265 ATN or RSC axon stimulation, were compared to responses elicited when both sets of axons  
266 were activated at short time intervals (dual; Figure 4A). The mean amplitude of dual oEPSPs  
267 (synchronous light onset, Figure 4A-C) was significantly larger than calculated summed  
268 amplitudes of single oEPSPs ( $n = 11$  cells, dual/summed amplitude  $2.06 \pm 0.55$  mV,  $p =$

269 0.0068, Wilcoxon test). Charge transfer, quantified as the surface under the dual oEPSP, was  
270 greater than the summed values for single oEPSPs (Dual/summed surface  $2.21 \pm 0.54$  mV.s,  $n$   
271  $= 11$ ,  $p = 0.0098$ , Wilcoxon test). These mean values cover variability between individual  
272 neurons. Summation of responses to ATN and RSC axon stimuli was supralinear in 7 out of 11  
273 cells tested, linear for 3 cells and sublinear for 1 cell.

274 Dynamic responses to repetitive stimulations were also transformed by dual  
275 photostimulation. Amplitudes of 5 dual oEPSPs elicited at 20 Hz were higher than for a linear  
276 summation (Amplitudes in mV, Summed vs. Dual: Stim 1,  $7.7 \pm 1.9$  vs.  $11.1 \pm 1.9$ ; Stim 2,  $6.7$   
277  $\pm 1.6$  vs.  $9.5 \pm 1.5$ ; Stim 3,  $6.5 \pm 1.4$  vs.  $9.5 \pm 1.5$ ; Stim 4,  $6.1 \pm 1.3$  vs.  $9.2 \pm 1.5$ ; Stim 5,  $5.9 \pm$   
278  $1.3$  vs.  $8.6 \pm 1.4$ ,  $p = 0.0117$ , Two-way ANOVA; Figure 4E) and charge transfer, quantified as  
279 the surface under the 5 oEPSPs, also typically summed supralinearly (20 Hz, Surface in mV.s,  
280 Summed vs. Dual: Stim 1,  $136.9 \pm 30.6$  vs.  $221.2 \pm 41.5$ ; Stim 2,  $143.3 \pm 25.7$  vs.  $242 \pm 43.9$ ;  
281 Stim 3,  $147.3 \pm 22.5$  vs.  $259.2 \pm 44$ ; Stim 4,  $145.1 \pm 22$  vs.  $263.5 \pm 49.2$ ; Stim 5,  $145.6 \pm 23.2$   
282 vs.  $258.7 \pm 45.2$ ,  $p = 0.0128$ , Two-way ANOVA; Figure 4F). Trains of dual ATN and RSC fiber  
283 stimulations also showed increased oEPSP integrals, compared to the stimulation of either  
284 one set of fibers alone, indicating stronger excitation over time (Figure 4E, F). Taken  
285 together, these data show supralinear summation of ATN and RSC inputs in most single layer  
286 3 pyramidal cells, and also a facilitation of dynamic responses to repetitive inputs at 20 Hz.

287 We next asked how efficiently action potentials were induced by combined ATN and  
288 RSC inputs. Firing probability of layer 3 cells was higher for dual than for single input  
289 stimulation at a membrane potential of -65 mV (ATN 0.008 vs Dual 0.268,  $n = 5$ ,  $p = 0.0216$ ,  
290 RSC 0.024 vs Dual 0.268,  $n = 5$ ,  $p = 0.1195$ , Friedman's and Dunn's tests) and higher still at -  
291 55 mV (Figure 4G, H). Firing was induced over a narrow window of time delays between  
292 stimulation of the two inputs (Figure 4I, J). It occurred for delays of -2 to +5 ms (RSC  
293 preceding ATN stimulus) reaching a maximum at a delay of +1 ms.

294 Supralinear summed responses of excitatory synaptic events may be mediated via  
295 the activation of NMDA receptors or voltage dependent intrinsic currents that amplify EPSPs  
296 (Fricker and Miles, 2000), especially if synaptic inhibition is reduced. We assessed these  
297 mechanisms in records made from layer 3 pyramidal neurons using a Cesium-based internal  
298 solution to favor cationic amplifying currents, and also containing QX314 to suppress action  
299 potentials (Figure 5). In 3 cells photostimulation of ATN fibers evoked oEPSPs of amplitude  
300  $10.9 \pm 2.0$  mV and RSC fiber stimulation induced events of  $13.7 \pm 2.5$  mV. The response  
301 dynamics to 5 light pulses at 20 Hz were moderately facilitating (2nd vs 1st amplitude ratio:  
302 ATN 1.39, RSC 1.17; 5th vs 1st: ATN 1.18, RSC 1.20;  $n = 3$ ). Coincident activation of ATN and  
303 RSC afferents induced supralinear oEPSP summation. Furthermore, repetitive stimulation  
304 generated large all-or-none depolarizations on the second or third stimulus at 20 Hz (2nd vs  
305 1st amplitude ratio: 1.52; 5th vs 1st: 2.90;  $n = 3$  cells, Figure 5A). It may be mediated by  
306 VGCC or a QX-314 resistant  $\text{Na}^+$  inward current (Fricker et al., 2009). This component  
307 appeared with higher probability and shorter latency in the presence of  $\text{GABA}_A$  receptor  
308 blocker gabazine (Figure 5B). The NMDA receptor antagonist APV largely abolished the dual  
309 EPSP amplification initially (Figure 5C, black trace; 2nd vs 1st integral ratio: 1.22; 5th vs 1st:  
310 1.32), although amplification was partially restored by increasing RSC stimulus intensity (pale  
311 pink trace). NMDA receptor activation thus assists depolarization towards the threshold of a  
312 voltage-dependent process contributing to supra-linear EPSP summation, but is not the only  
313 charge carrier involved.

314

315 **Cholinergic modulation and recruitment of presubicular layer 4 neurons by ATN and RSC**  
316 **afferents**

317 Presubicular layer 4 neurons are intrinsic bursting pyramidal neurons that project to  
318 the lateral mammillary nucleus (Huang et al., 2017). This pathway is critical for the  
319 coordinated stable landmark control of HD cells in the thalamus and throughout the HD cell  
320 circuit (Yoder et al., 2015; Yoder et al., 2017) To investigate the input connectivity of layer 4  
321 principal cells, we recorded responses of these neurons to stimulation of ATN and RSC  
322 afferents.

323 Layer 4 neurons labeled by retrograde tracers injected in the lateral mammillary  
324 nucleus were located in the *lamina dissecans* of the presubiculum, below layer 3, where  
325 thalamic axons ramify (Figure 6A-D). The apical dendrites of layer 4 pyramidal neurons  
326 extended towards presubicular layer 1 as previously described (Huang et al., 2017), but  
327 tended to circumvent layer 3 and avoid thalamic afferents, by swerving towards the  
328 subiculum. Apical dendrites of some neurons crossed layer 3 obliquely, while others avoided  
329 thalamic afferents in layer 3 (Figure 6C, D, Figure 6—figure supplement 1).

330 Layer 4 neurons had a more depolarized resting membrane potential, lower input  
331 resistance and time constant than layer 3 neurons (Figure 6—figure supplement 2 compares  
332 active and passive properties). A characteristic voltage sag in responses to hyperpolarizing  
333 steps, indicated the presence of an  $I_h$  current. Layer 4 neurons discharged bursts of two or  
334 three action potentials at the onset of a depolarizing step current injection and also after the  
335 offset of hyperpolarizing steps (Figure 6E). These bursts were abolished by the T-type  $Ca^{2+}$   
336 channel blocker TTA-P2 (Figure 6F).

337 We next recorded responses of layer 4 neurons to optical activation of ATN or RSC  
338 afferents together with effects of the same stimuli on layer 3 pyramidal cells (Figure 6G).  
339 Overall, latencies of oEPSCs in layer 4 neurons were longer than for layer 3 (ATN layer 4,  $6.2$   
340  $\pm 0.6$  ms,  $n = 8$ , vs. layer 3,  $2.4 \pm 0.2$  ms,  $n = 24$ ; RSC layer 4,  $5.6 \pm 0.4$  ms,  $n = 9$ , vs. layer 3,  
341  $2.9 \pm 0.2$  ms,  $n = 27$ ; Figure 6H), indicating possible polysynaptic excitation of layer 4  
342 neurons. Bath application of TTX-4AP did not abolish oEPSPs entirely, leaving a low  
343 amplitude component with short, potentially monosynaptic latencies (latency ATN  $3.9 \pm 0.6$   
344 ms, RSC  $2.9 \pm 0.2$  ms,  $n = 5$ ; Figure 6I).

345 Comparison of the timing of synaptic events and firing (Fig 7A-C) showed that oEPSP  
346 onset in a layer 4 neuron occurred after firing in the layer 3 neuron, for either ATN (4/5) or  
347 RSC (1/1) afferent stimuli. Depolarization of the layer 3 cell via the patch pipette, initiated  
348 firing, but EPSPs were not elicited in any simultaneously recorded layer 4 neuron (0 out of 6  
349 cell pairs tested). These data suggest that excitation of layer 3 cells by ATN and RSC afferents  
350 is transmitted to layer 4 neurons, even in the absence of direct evidence for mono-synaptic  
351 coupling between cell pairs.

352 In records from pairs of layer 3 and 4 neurons ( $n = 3$ ; Figure 7D, E) layer 3 cells  
353 responded with precisely timed action potentials to low intensity stimulation of ATN  
354 afferents, while only very small oEPSPs were initiated in layer 4 neurons. Increasing the  
355 excitatory drive by stimulating RSC afferents elicited larger oEPSPs more reliably in layer 4  
356 neurons. Higher intensity stimulation of both ATN and RSC axons, could evoke bursts of  
357 action potentials, with the activation of an underlying  $Ca^{2+}$  current in layer 4 cells (Figure 7E).  
358 We hypothesize that increasing the activity of layer 3 neurons by strong (and non-specific)  
359 stimulation of ATN and RSC afferents is needed to induce discharges in layer 4 cells. We  
360 should also note that strong photostimulation of a single set of afferent fibers could initiate

361 discharges in layer 4 pyramidal cells, as was shown in records from mice where only one  
362 afferent brain area, ATN or RSC, expressed an opsin (Figure 7—figure supplement 1).

363 Overall, it seems probable that layer 3 neurons relay activity projected by ATN and  
364 RSC inputs onto layer 4 pyramidal neurons. However, evidence on this point could be  
365 improved. In dual records, we did not detect functional synapses between layer 3 and layer 4  
366 neurons (n = 9). Anatomically, putative synaptic contacts between filled axons of layer 3 and  
367 dendrites of layer 4 cells, were not evident (n = 5 filled layer 4 cells; see also Peng et al.,  
368 2017). We did find a possible synaptic connection between two neighboring L4 neurons in  
369 one case (Figure 6—figure supplement 1D), with a close apposition between axon and  
370 dendrite. Recurrent excitation may promote bursting in a positive feedback loop in layer 4  
371 neurons, and NMDA receptor related EPSP amplification favors burst firing (Figure 7F).

372 Neuromodulatory factors may help drive layer 4 cells to fire action potentials. As  
373 Presubiculum is rich in acetylcholinesterase (Slomianka and Geneser 1991), we examined  
374 excitability changes in the presence of a broad cholinergic agonist. The application of  
375 Carbachol (10  $\mu$ M; Figure 7G) led to a depolarization of the recorded layer 4 neurons'  
376 membrane potential by  $13 \pm 4$  mV, with increased action potential firing during a positive  
377 step current injection, and from the baseline (Figure 7Gi,ii). The depolarizing effect of  
378 carbachol was mimicked by muscarine (10  $\mu$ M; n = 3), and persisted in the presence of TTX  
379 (1  $\mu$ M; n = 2), indicating a direct effect on layer 4 neurons.

380  
381  
382  
383  
384

## 385 Discussion

386  
387  
388  
389  
390  
391  
392  
393  
394  
395  
396  
397  
398  
399  
400  
401  
402  
403

Understanding the anchoring of HD signals with visual landmarks provides a useful  
framework to ask how external information is integrated to revise and improve brain  
representations. Here we show that thalamic ATN afferents signaling HD data and cortical  
RSC projections that carry visual landmark information converge on layer 3 pyramidal cells of  
the dorsal presubiculum. Independent optogenetic stimulation of these two glutamatergic  
afferents in slices was used to define mechanisms of their integration in the presubiculum.  
Most layer 3 cells were innervated by both ATN and RSC fibers, sometimes close on the same  
dendritic branches, sometimes on different dendrites. Nearly coincident EPSPs (2-5 ms)  
induced independently by ATN and RSC afferents, evoked non-linear membrane responses  
to trigger layer 3 cell firing, transmitted to the MEC. In a second processing step, layer 3  
neurons also excite layer 4 pyramidal cells which receive little direct ATN and RSC  
innervation. These burst firing neurons, project a distinct, di-synaptically mediated, visually-  
updated HD signal to the LMN. Our data thus suggest that the presubiculum integrates HD  
and landmark signals producing two distinct output signals which are transmitted to  
different regions. Cholinergic modulation may facilitate responses to salient stimuli, for  
flexible anchoring to landmarks.

### 404 *Anatomical convergence of ATN and RSC projections in the dorsal Presubiculum*

405 Retrograde tracing in this study confirmed strong projections to the presubiculum  
406 from the ATN and the RSC to the presubiculum (Figure 1). Anterior thalamic fibers

407 (Van Groen et Wyss 1990c; 1990a; 1990b; 1992; Shibata et Honda 2012; Vogt et Miller 1983)  
408 ramify in and delimit the anatomical borders of the presubiculum (Liu et al., 2021; Simonnet  
409 et al., 2017). HD signals from HD cells of the anterior thalamus project to the presubiculum  
410 (Goodridge and Taube, 1997) where they form synapses directly with layer 3 pyramidal cells  
411 (Nassar et al., 2018). The retrosplenial cortex was the most strongly labeled cortical region  
412 innervating the presubiculum. We detected retrogradely transported beads in cells of layers  
413 2 and 5 of dysgranular RSC, and layer 5 of the granular RSC across its antero-posterior axis  
414 (Sugar and Witter, 2016).

415 We examined the anatomy and physiology of these two afferent systems to ask how visual  
416 landmark signals from the RSC are combined with HD signals relayed via the ATN.  
417 Anterograde fiber tracing, with an AAV5 construct expressing Chronos-GFP, confirmed that  
418 axons from both regions project to superficial layers of the dorsal presubiculum. No RSC  
419 projections were found in ventral PrS for injections in rostral RSC, as previously noted (Jones  
420 and Witter 2007; Kononenko and Witter 2012). Both RSC and ATN innervated superficial  
421 presubicular layers 1 and 3, while sparing layer 2 containing somata of calbindin positive  
422 neurons (Figure 1K and cf. Balsamo et al. 2022). We detected microzones containing a high  
423 density of ATN-positive fibers, but no RSC fibers, in upper layer 3.

424

425 *Pathway specific functional connectivity onto PrS layer 3 neurons.*

426 Photostimulation of GFP-Chronos expressing axons let us compare synaptic events  
427 initiated in layer 3 pyramidal cells by fibers from the ATN or the RSC in dorsal presubiculum  
428 slices (Figure 2). Both ATN and RSC afferents formed mono-synaptic glutamatergic  
429 connections with components mediated by NMDA and AMPA receptors. The amplitudes of  
430 synaptic currents varied, with an overall similar amplitude distribution for ATN and RSC  
431 stimulation. This may be due to variable expression levels (Hooks et al. 2015), or may imply  
432 variations in coupling weights across cells. ATN and RSC fiber mediated EPSCs depressed  
433 during repetitive activation at 20 Hz. EPSPs induced firing early during repetitive stimulation.  
434 RSC inputs tended to produce more sustained EPSP dynamics and slower rise times than ATN  
435 afferents for low intensity stimulation. ATN synapses with presubicular pyramidal cells  
436 resemble those made by thalamic afferents in the somatosensory cortex - high release with  
437 depressing dynamics, (Gil et al., 1999) possibly due to presynaptic expression of VGLut2 (Liu  
438 et al., 2021).

439 Dual wavelength optogenetic stimulation was used for independent activation of  
440 intermingled afferents expressing blue-light sensitive Chronos in ATN fibers and red-shifted  
441 Chrimson in RSC fibers (Klapoetke et al., 2014). Precautions were taken to avoid cross-  
442 stimulation since all channelrhodopsin variants are somewhat sensitive to blue light. With  
443 the fast, sensitive opsin Chronos expressed in ATN fibers, synaptic events were induced by  
444 very short (0.5 ms), low intensity, 0.25 mW, stimuli. For RSC fibers expressing Chrimson,  
445 using light stimuli of duration 2 ms, adjusting intensity up to 2 mW initiated synaptic events  
446 of comparable amplitude. Calibration experiments (Figure 3—figure supplement 1) provided  
447 strong evidence for the independence of responses. While Chrimson has slower dynamics  
448 than Chronos (Klapoetke et al., 2014), synaptic events induced by stimulating either opsin  
449 were similar, as we showed by swapping the two opsin variants injected in ATN and RSC  
450 fibers respectively (Figure 4).

451 This dual opsin approach permitted independent stimulation with blue and red light  
452 pulses. Most (76%) recorded layer 3 neurons generated synaptic events in response to  
453 stimulation of both ATN and RSC fibers providing a substrate for integration of landmark

454 information from the RSC with thalamic HD signals. Layer 3 cell firing was most effectively  
455 triggered by nearly coincident inputs (-2 to +5 ms separation, Figure 4I, J). This is of interest  
456 since HD representations in the AD and RSC are highly coherent (Fallahnezhad et al., 2023),  
457 with short intervals between spikes in these two regions (< 5ms; van der Goes et al. 2022).  
458 Converging inputs from thalamic and retrosplenial axons can therefore excite common  
459 postsynaptic presubicular layer 3 neurons with very short delays, such that coincidence  
460 detection by these cells will tend to enhance HD signals transmitted to the MEC. Response  
461 dynamics to combined stimulation of both inputs at 20 Hz were maintained or facilitating, in  
462 contrast to the depressing dynamics of repetitive stimulation of one set of afferent fibers.  
463 Combined and temporally precise inputs from ATN and RSC may thus help maintain HD  
464 signaling during immobility.

465

#### 466 *Nonlinear signal integration in layer 3 thalamo-recipient neurons*

467 Convergence of ATN and RSC axons onto single layer 3 pyramidal cells provides the  
468 anatomical basis of synaptic integration. Putative synaptic contacts from both afferent fiber  
469 systems were found on the basal dendrites of pyramidal cells (Figure 3), sometimes on the  
470 same branch. Photostimulation centered on the soma of recorded neurons predominantly  
471 activated synapses on basal dendrites. Supralinear summation could result from local spike-  
472 generating mechanisms if the activated synapses were located on a same dendritic branch  
473 (Makarov et al., 2023; Poirazi and Papoutsi, 2020; Polsky et al., 2004). Clustered synapses  
474 could also guide the formation of new spines and synapses during integration of landmark  
475 information in the HD signal. Learning might bind new inputs into functional synaptic  
476 clusters (Hedrick et al., 2022). Our small sample of layer 3 pyramidal cells suggest that both  
477 ATN and RSC axons target basal dendrites, and more RSC than ATN axons contact apical  
478 dendrites (Figure 3). Tests on the effects of precise, near coincident activation of basal and  
479 apical synapses could be revealing but were not technically possible in this study. Distinct  
480 dendritic inputs to layer 3 cells may improve spatial perception (Takahashi et al., 2016)  
481 enhancing HD signal quality by integration with landmark information.

482

483 Our data show that EPSPs elicited by nearly coincident ATN and RSC inputs which  
484 exceed a threshold are amplified by NMDA receptor activation and voltage gated inward  
485 dendritic currents (Figure 5; Fricker et al. 2009). EPSP amplification is facilitated by a  
486 reduction in synaptic inhibition (Figure 5), indicating that disinhibition may be permissive for  
487 supralinearity and gate firing by dynamic modulation of the balance between inhibition and  
488 excitation (Milstein et al., 2015). VIP expressing interneurons, which are excited by  
489 cholinergic modulation could provide such disinhibition of the presubicular microcircuit  
490 (Porter et al., 1999; Slomianka and Geneser, 1991). A 'when-to-learn' signal for HD updating  
491 in the presubiculum might function analogously to the promotion by dopamine of  
492 associations between sensory cues and head direction cells in the fly compass neurons  
493 (Fisher et al., 2022). It is however unclear whether LTP type learning takes place in the  
494 mammalian head direction circuit. Presubicular layer 3 cells do not express the GluR1  
495 subunit of AMPA receptors (Martin et al 1993; Ishihara et al., 2016) that is critical for LTP  
496 expression (Boehm et al., 2006). The absence of GluR1 might indicate that the thalamo-  
497 presubicular synapses in layer 3 function without classical long-term plasticity.

497

498 Layer 3 pyramidal cells may be described as multi-compartmental computational  
499 devices (Häusser and Mel, 2003; Mel, 1993; Poirazi et al., 2003; Spruston, 2008) which  
500 integrate HD and landmark information. ATN axons drive presubicular HD neurons (Peyrache  
et al., 2015) and RSC mixed selectivity neurons contribute visual landmark information and

501 allocentric spatial references (Jacob et al., 2017; Mitchell et al., 2018; Vann et al., 2009).  
502 NMDA mediated dendritic spikes enhance tuning selectivity in visual cortex (Smith et al.,  
503 2013; Wilson et al., 2016) and barrel cortex (Lavzin et al., 2012). Dendritic events in Layer 3  
504 PrS cells may enable binding of visual landmarks with HD tuning. It is tempting to speculate  
505 that nonlinear synaptic integration and inhibitory gating may be involved in flexibly updating  
506 the allocentric direction of HD cells based on the integration of visual landmark information  
507 to the current HD signal. In the primary sensory cortex, nonlinearities act to increase  
508 perceptual threshold of sensory information (Takahashi et al., 2016; 2020). The attractor  
509 network in the PrS could thus be either stabilized or flexibly reset to external spatial cues.

510  
511  
512

### 513 *Functional significance of two-layer processing preceding projection to LMN*

514 Burst-firing layer 4 PrS cells project a distinct version of HD-landmark signals to the  
515 LMN. The dendrites of these LMN projecting neurons overlap little with direct ATN and RSC  
516 inputs granting partial isolation from direct excitation, and permitting a second level of  
517 integration of information from layer 3 neurons. Layer 3 axons may innervate layer 4  
518 neurons basal dendrites, which may be driven to fire by sufficiently strong excitatory inputs  
519 from layer 3, especially if combined with cholinergic activation.

520 There are advantages to segregating the integration of converging input signals from  
521 the updating signal across layers. This separation permits both a fast transmission of an  
522 integrated signal to the medial entorhinal cortex, and the conditional transmission of a  
523 updating signal mediated by burst firing to upstream HD circuit elements. The synaptic  
524 threshold implicit in this two-stage system permits a gated updating. Functionally layer 4  
525 neurons are uniquely positioned to update the HD signal in the LMN with visual landmark  
526 information (Yoder et al., 2015). In this way, cell-type specific cholinergic facilitation may  
527 help idiothetic cue based navigation (Yoder et al., 2017). These cellular and synaptic circuit  
528 data support and expand the findings of Yoder et al. (2015 and 2017). They clarify how the  
529 thalamic HD signal integrated with visual landmark information is relayed to the grid cell  
530 system in the medial entorhinal cortex and to the lateral mammillary nuclei.

531  
532

### 532 *Limitations*

533 Burst firing may play a role for learning in hierarchical circuits (Naud et al., 2023; Payeur et  
534 al., 2021). In the HD circuit, visual landmark information contained in bursts might reset or  
535 anchor the HD attractor in the LMN and beyond. The effects of burst firing signals  
536 transmitted to the LMN remain to be assessed. Potentially HD signals may be updated with  
537 visual signals at several sites including the PrS, but this region uniquely provides a feed-back  
538 projection to the lateral mammillary nucleus. Further work on layer 3 to layer 4 transmission  
539 is warranted, and the link to spatial perception and behavioural updating needs to be  
540 strengthened.

541

## 542 **Methods**

543

### 544 **Animals**

545 Experiments were performed on wild-type and transgenic C57Bl6 mice, housed on a  
546 12 hours light/dark cycle with food and water available *ad libitum*. Animal care and use



547 conformed to the European Community Council Directive (2010/63/EU) and French law  
548 (87/848). Our study was approved by the local ethics committee (CEEA - 34) and the French  
549 Ministry for Research 01025.02.

550

#### 551 **Viral vectors and beads**

552 Projecting neurons were labeled with retrograde fluorescent tracers (Retrobeads,  
553 Lumafluor, and pAAV-CAG-tdTomato, Addgene 59462P). Fluorescent beads were stored at  
554 4°C before use. Channelrhodopsin expression was achieved by injecting Adeno-associated  
555 viral constructions. AAV5.Syn.Chronos-GFP.WPRE.bGH (AAV5-Chronos, Penn Vector Core,  
556 Addgene 59170P) was used to induce neuronal expression of the blue light induced  
557 channelrhodopsin Chronos fused to the GFP marker and under the control of the Synapsin  
558 promoter. AAV5.Syn.ChrimsonR-tdTomato.WPRE.bGH (AAV5-Chrimson, Penn Vector Core,  
559 Addgene 59171P) induced neuronal expression of the red light gated channelrhodopsin  
560 Chrimson fused to the tdTomato marker, under the control of the Synapsin promoter. Viral  
561 vectors were stored at -80°C before use.

562

#### 563 **Stereotaxic surgery**

564 Mice at ages of 4-5 weeks were anesthetized by intraperitoneal (i.p.) injection of a  
565 mixture of ketamine hydrochloride and xylazine (100 and 15 mg/kg respectively, in NaCl  
566 0.9%). They were placed in a stereotaxic frame for injections. Fluorescent beads for  
567 retrograde tracing were injected (300-500 nl) into the PrS at the coordinates: -4.06 antero-  
568 posterior (AP), 2.00 medio-lateral (ML) and -2.15 mm dorso-ventral (DV) and into the LMN (-  
569 2.8 AP, 0.75 ML, -5.35 DV) with respect to the bregma.

570 Viral injections were performed unilaterally (Mathon et al., 2015; Richevaux et al., 2019) at  
571 the coordinates -0.82 AP, 0.75 ML and -3.2 mm DV for the ADN, and at -2.1 to -2.15 AP, 0.65  
572 ML and -0.65 mm DV for the RSC. Volumes of 200 to 250 nl were injected with a 10 µL  
573 Hamilton syringe equipped with 33ga needle over a time of 10 min. The needle was slowly  
574 removed after a delay of 10 min to avoid leakage from the injection site. Best expression of  
575 AAV5 serotypes was achieved after 3 to 4 weeks.

576

#### 577 **Tissue fixation and slicing for retrograde tracing**

578 Brains were removed for anatomy at 4 days after retrobead injection. Mice were  
579 anesthetized by i.p. injection of the ketamine/xylazine mixture. An intracardiac perfusion  
580 with 0.1M PBS was followed by perfusion with 4% paraformaldehyde. Brains were stored  
581 overnight in paraformaldehyde at 4°C and then washed in PBS. Coronal or horizontal  
582 sections were cut at 100 µm with a vibratome and stored in sucrose at 4°C.

583

#### 584 **Preparation of brain slices for physiology**

585 Slices of the temporal lobe were prepared 3-4 weeks after injection of AAV5 viral  
586 constructions. Mice were anesthetized by i.p. injection of the ketamine/xylazine mixture.  
587 They were then perfused intracardially with a cutting solution containing (in mM): 125 NaCl,  
588 25 sucrose, 2.5 KCl, 25 NaHCO<sub>3</sub>, 1.25 NaH<sub>2</sub>PO<sub>4</sub>, 2.5 D-glucose, 0.1 CaCl<sub>2</sub>, 7 MgCl<sub>2</sub>, cooled to  
589 4°C, and oxygenated with a 5% CO<sub>2</sub> / 95% O<sub>2</sub>. The brain was removed and a vibratome was  
590 used to cut horizontal slices at 300 µm in the same solution. Slices were stored for 15 min at  
591 34°C in an ACSF containing (in mM): 124 NaCl, 2.5 KCl, 26 NaHCO<sub>3</sub>, 1 NaH<sub>2</sub>PO<sub>4</sub>, 2 CaCl<sub>2</sub>, 2  
592 MgCl<sub>2</sub>, and 11 D-glucose, bubbled with 5% CO<sub>2</sub> / 95% O<sub>2</sub>. They were then kept in the same  
593 solution at room temperature until recording.

594

595 **Whole-cell patch-clamp recordings**

596 Slices were transferred to a recording chamber perfused with oxygenated, warmed  
597 (~32 °C) ACSF mounted on an epifluorescence microscope. Patch-clamp records were made  
598 from neurons with borosilicate glass pipettes of external diameter 1.5 mm (Clark Capillary  
599 Glass, Harvard Apparatus) pulled with a Brown-Flaming electrode puller (Sutter  
600 Instruments). Electrodes, filled with a potassium-gluconate based solution containing (in  
601 mM): 135 K-gluconate, 1.2 KCl, 10 HEPES, 0.2 EGTA, 2 MgCl<sub>2</sub>, 4 MgATP, 0.4 Tris-GTP and 10  
602 Na<sub>2</sub>-phosphocreatine, had a resistance of 4-8 MΩ. An alternative, cesium-gluconate based  
603 solution facilitated neuronal depolarization to examine synaptic inhibition. It contained (in  
604 mM): 125 Cs-gluconate, 10 HEPES, 0.2 EGTA, 2 MgCl<sub>2</sub>, 4 MgATP, 0.4 Tris-GTP and 10 Na<sub>2</sub>-  
605 Phosphocreatine, together with 5 mM QX-314 to block Na<sup>+</sup> channels. Pipette solutions also  
606 contained 3 mM biocytin to reveal morphology after recording. They were adjusted to pH  
607 7.3 and osmolarity 290 mOsm. Whole-cell, patch-clamp signals were filtered at 3kHz,  
608 amplified with a MultiClamp 700B amplifier and acquired with pCLAMP software (Molecular  
609 Devices). Monosynaptic excitation induced by optical stimulation was tested in the presence  
610 of TTX (1 μM) and 4-AP (100 μM). NBQX (10 μM) and APV (100 μM) were used to block  
611 AMPA and NMDA receptors respectively. Gabazine (10 μM) was used to block GABA<sub>A</sub>  
612 receptors. Carbachol (10 μM) was used to activate acetylcholine receptors. All drugs were  
613 bath applied.

614

615 **Optical stimulation**

616 LED illumination (Cairn Research, OptoLED) was used to visualize the fluorescent  
617 reporters GFP and tdTomato, and to stimulate opsin-expressing axons, using a 470 nm LED  
618 for Chronos and a 627 nm LED for Chrimson. Illuminated spots had a diameter of 200 μm  
619 with a 60x objective and were centered on the recorded cell soma. Photostimulation thus  
620 covered most of the basilar dendrites of layer 3 pyramidal neurons (typical distance from tip  
621 of apical to tip of basilar dendrite <400μm). Stimuli consisted of light pulses of 0.5 to 5 ms  
622 duration, repeated 5-10 times at 20 Hz.

623

624 A multiband filter allowed simultaneous stimulation by blue and red LEDs of axons  
625 containing Chronos and Chrimson (Simonnet et al., 2021). Stimulus power intensity (set in  
626 mV) was calibrated as light intensity. The response probability of layer 3 cells was calibrated  
627 to blue or red illumination of ATN or RSC afferents expressing Chronos or Chrimson to avoid  
628 stimulus overlap (Figure 3—figure supplement 1). Chronos was targeted to the ATN and  
629 Chrimson to the RSC after testing the reverse configuration. Projections from the thalamus  
630 are larger and Chronos is more sensitive to blue light, so this configuration assured reliable  
631 activation of thalamic fibers at minimal blue-light intensities. For experiments investigating  
632 the integration of ATN and RSC inputs, we aimed to give similar weights to both inputs:  
633 Chrimson-expressing fibers were stimulated with light of intensity adjusted to initiate  
634 optically evoked excitatory postsynaptic potentials (oEPSPs) of amplitude similar to those  
635 induced by blue light Chronos-fiber stimuli.

635

636 **Data analysis**

637 ATN and RSC projections to the PrS, were analyzed from Chronos and Chrimson  
638 expression, using the ImageJ Plot Profile plug-in to quantitate normalized plot profiles (2000  
639 pixels) of horizontal presubicular sections. Dorso-ventral differences were derived by  
640 dividing differences in labeling intensity between the PrS and the dentate gyrus (DG)

641 molecular layer by DG intensity in slices from 5 dorso-ventral PrS levels. Values from all  
642 animals were averaged and then normalized.

643 Cells were qualified as synaptically 'connected' when they responded to light  
644 stimulation of afferent axons with a delay < 8 ms. Slices with very low or absent expression  
645 of the fluorescent reporter were excluded. Cells were qualified as 'non-connected'  
646 synaptically, if they did not respond to light stimulation, but at least one neighboring cell in  
647 the same slice did.

648 Intrinsic neuronal properties were analyzed with custom MATLAB routines to derive  
649 15 electrophysiological parameters (Huang et al., 2017). Parameters were standardized and  
650 unsupervised cluster analysis performed with MATLAB was used to compare different  
651 neurons (Huang et al., 2017; Simonnet et al., 2013).

652 Axograph was used to analyze responses to optical stimulation of ATN and RSC fibers.  
653 Layer 3 neurons were recorded at potentials near -65 mV. Responses to light were averaged  
654 from 10 stimulus trains at 20 Hz. Amplitudes and latencies of initial light evoked EPSCs, of  
655 latency shorter than 10ms, were quantified from voltage-clamp records. Latency was  
656 measured from stimulus onset to 10% of the peak amplitude of the first optically induced  
657 EPSC. Amplitude was measured with respect to the pre-stimulus baseline. Paired-pulse ratio  
658 (PPR) was defined as the ratio of the amplitude of the second to the first EPSC and 10/1 ratio  
659 as that between the 10th and the 1st EPSC, in responses to 20 Hz stimulations. Spike  
660 probability was counted over 5 to 10 trials per cell and then averaged over all cells. EPSPs  
661 induced by dual wavelength stimulation were analyzed using Axograph and a custom-made  
662 software. Events evoked by light stimuli were detected in a window of 1-10 ms after  
663 stimulation. EPSP amplitude and integrated area were calculated over 50 ms after  
664 stimulation. Baseline suppression was applied using an average of membrane potential  
665 during 50 ms before stimulation. Summation of ATN and RSC evoked EPSCs in layer 3  
666 neurons was determined from the amplitude and integral of averaged events. Summation  
667 was considered to be supralinear, if values were more than 10% higher than a linear  
668 addition, linear for values within  $\pm 10\%$ , and sublinear for values more than 10% lower.

669

#### 670 **Biocytin revelation and morphology**

671 Recorded neurons were filled with biocytin to visualize their morphology and  
672 location. Slices were fixed in 4% PFA in 0.1 M PBS at 4°C overnight, washed 3 times in 0.1  
673 PBS and cryoprotected in 30% sucrose. Cell membranes were permeabilized by three freeze-  
674 thaw cycles over dry ice and rinsed in PBS. Slices were agitated in a saturation buffer (2%  
675 milk, 1% Triton X-100 in 0.1 M PBS) for 2 hours at room temperature. They were then  
676 incubated with Streptavidin-Cy5 conjugate (1:500) and DAPI (1:1000) overnight at 4°C.  
677 Sections were washed 3 times with PBS and mounted on coverslips with ProLong gold  
678 antifade mountant. For anatomical study they were mounted in Mowiol medium. Cell, bead  
679 and virus expression were visualized with an epifluorescence microscope. Higher resolution  
680 of morphology was obtained with confocal microscopy. Cell morphologies were  
681 reconstructed using IMARIS.

682

#### 683 **Quantification and statistical analysis**

684 Data was analyzed with AxoGraphX and custom-written software (MATLAB, The  
685 MathWorks). Results are given as mean  $\pm$  SEM. Statistical analysis was performed with Prism  
686 (GraphPad Software). The Mann-Whitney unpaired t-test was used to compare two groups.  
687 The Wilcoxon or Kruskal-Wallis test was used to compare paired groups. Evolution of

688 parameters evoked by optical stimulation (current or potential amplitudes, spike probability)  
689 was analyzed with Friedman's test followed by multiple comparison Dunn's test. Šidák's  
690 multiple comparison test was also used to compare linear and observed responses to ATN  
691 and RSC stimulations. Significance levels are given as p values.

692  
693  
694

## 695 **Acknowledgements**

696

697 This work is supported by the Centre National de la Recherche Scientifique and the  
698 Université Paris Cité. DF received funding from the Agence Nationale de la Recherche (ANR-  
699 DFG Program, ANR-18-CE92-0051 BURST), from the ERA-NET NEURON Program (ANR-20-  
700 NEUR-0005 VELOSO), and the FLAG-ERA HBP Program (ANR-21-HBPR-0002 VIPattract). This  
701 work has benefited from support by the BioMedTech Facilities at Université Paris Cité  
702 (Institut National de la Santé et de la Recherche Médicale Unité S36/Unité Mixte de Service  
703 2009). We thank Dr. Li-Wen Huang for help with analysis routines. We thank Dr. Kate Jeffery  
704 and the Royal Society COST-share program, technical assistance from Fabrice Licata from the  
705 UPC Microscopy platform, Claire Lovo from ICM Quant, Dr. Boris Lamotte d'Incamps, and  
706 Dr. Richard Miles for helpful comments on the manuscript.

707

## 708 **Author contributions**

709 L.R. and D.F. conceived experiments, designed study, and interpreted data. D.F.  
710 acquired funding, L.R. and D.F. managed the project. L.R., D.L., M.N., C.M., L.D-R. and N.S-F.  
711 performed experiments and analyzed data, I.C. helped with analysis software, L.R. and D.L.  
712 prepared figures, L.R. and D.F. wrote the manuscript.

713

## 714 **Declaration of Interests**

715 The authors declare no competing financial interests.

716

## 717 **Figure titles and legends**

718 **Figure 1** with 1 supplement.

719 **ATN and RSC send strong axonal projections to the superficial layers of dorsal**  
720 **Presubiculum**

721 A, Retrograde labeling of cortical and subcortical regions projecting to the presubiculum  
722 (PrS) with retrobeads.

723 B, Ipsilateral anterodorsal and anteroventral thalamic nuclei are labeled with beads.

724 C, Ipsilateral granular (gRSC) and dysgranular (dRSC) retrosplenial cortex labeling. Scale bars  
725 B, C, 200  $\mu$ m.

726 D, Anterograde labeling of thalamic and retrosplenial projections to PrS with AAV-Chronos-  
727 GFP.

728 E, F, Injection sites in ATN (E) and RSC (F). AD: anterodorsal thalamic nucleus, AV:  
729 anteroventral thalamic nucleus, CA1: field of the hippocampus, cc: corpus callosum, cg:  
730 cingulum, CPu: caudate putamen, DG: dentate gyrus, MD: thalamic medial dorsal nucleus,

731 MEC: medial entorhinal cortex, PaS: parasubiculum, PVA: paraventricular thalamic nucleus,  
 732 anterior, Rt: thalamic reticular nucleus, sm: stria medullaris, Sub: subiculum, VL: thalamic  
 733 ventrolateral nucleus.  
 734 G, H, Five sequential 100- $\mu$ m horizontal slices of the parahippocampal region show ATN (G)  
 735 and RSC (H) axons expressing Chronos-GFP (green). Dashed lines show limits of the  
 736 parahippocampal region to the left and of the dentate gyrus to the right. Numbers show  
 737 dorsoventral level with respect to bregma. Scale bars 100  $\mu$ m.  
 738 I, Normalized profiles of fluorescent intensity for ATN and RSC projections to the  
 739 presubiculum, from white matter (WM) to pia (PIA). Mean (green)  $\pm$  SEM (grey), n = 8.  
 740 J, Ventral (V) to dorsal (D) normalized distribution of ATN and RSC projections to the  
 741 presubiculum, n = 3 mice.  
 742 K, ATN axon labeling (green) is segregated from calbindin labeling (white) in the PrS. Scale  
 743 bar 100  $\mu$ m.  
 744 See also Figure 1—figure supplement 1.

745

746 **Figure 1—figure supplement 1. Brain regions providing input to the Presubiculum.**

747 Semi-quantitative estimate of retrobeads labelling in serial coronal slices following injection  
 748 in the presubiculum. Color intensity represents beads density (mouse #69).

- 749 - Thalamic nuclei: anterodorsal (AD) +++, anteroventral (AV) +++, laterodorsal (LD)  
 750 +++, lateroposterior ++, dorsal lateral geniculate ++, reuniens ++, anteromedial -,  
 751 ventrolateral -
- 752 - Retrosplenial cortex: dysgranular (dRSC) +++, granular +++, dysgranular  
 753 contralateral ++
- 754 - Visual cortex: primary (V1) ++, secondary (V2L) +++
- 755 - Entorhinal cortex: lateral (LEnt) +++, medial (MEnt) +++
- 756 - Hippocampus/parahippocampus: parasubiculum (PaS) +++, subiculum (Sub) +++,  
 757 controlateral PrS ++, CA1 ++, CA3 -, dentate gyrus -
- 758 - Other: claustrum ++, perirhinal cortex ++, temporal association cortex ++

759

760 ADN: anterodorsal thalamic nucleus; AM: anteromedial thalamic nucleus; APT(V): anterior  
 761 pretecal nucleus (ventral part); AVDM: anteroventral thalamic nucleus, dorsomedial part;  
 762 AVVL: anteroventral thalamic nucleus, ventrolateral part; CA: cornu ammonis; cc: corpus  
 763 callosum; Cl: Claustrum; Cg1,2: cingular cortex area 1,2; coll. sup: colliculus superior; CPu:  
 764 caudate putamen (striatum); dhc: dorsal hippocampal commissure; DG: dentate gyrus; DLG:  
 765 dorsal lateral geniculate nucleus; LEnt: lateral entorhinal cortex; LDDM: laterodorsal thalamic  
 766 nucleus, dorsomedial part; LDVL: laterodorsal thalamic nucleus, ventrolateral part; LMN:  
 767 lateral mammillary nucleus; LS: lateral septal nucleus; M1,2: primary, secondary motor  
 768 cortex; MEnt: medial entorhinal cortex; MMN: medial mammillary nucleus; PAG:  
 769 periaqueductal gray; PaS: Parasubiculum; PF: parafascicular thalamic nucleus; PH: posterior  
 770 hypothalamic area; PMCo: posteromedial cortical amygdaloid nucleus; Po: posterior  
 771 thalamic nuclear group; PRh: perirhinal cortex; PrS: presubiculum; PVA: paraventricular  
 772 thalamic nucleus, anterior part; S1BF, S1FL, S1ULp, S1Tr: primary somatosensory cortex,  
 773 barrel field, forelimb region, upper lip region, trunk region; S2: secondary somatosensory  
 774 cortex; sm: stria medullaris of the thalamus; Sub: subiculum; Subst. Nigra: substantia nigra;  
 775 Re/Reuniens: reuniens thalamic nucleus; RSA = dRSC, dysgranular retrosplenial cortex; RSC:  
 776 retrosplenial cortex; RSG = gRSC: granular retrosplenial cortex; Rt: reticular thalamic nucleus;  
 777 V1: primary visual cortex; V2M: secondary visual cortex, medial part; V2L: secondary visual

778 cortex, lateral part; VA: ventral anterior thalamic nucleus; VDB: nucleus of the vertical limb  
779 of the diagonal band; VL: ventrolateral thalamic nucleus; VPL: ventral posterolateral thalamic  
780 nucleus; VPM: ventral posteromedial thalamic nucleus

781

782

783 **Figure 2** with 2 supplements.

784 **Responses of layer 3 presubicular cells to photoactivation of ATN and RSC fibers.**

785 A, Expression of AAV5-Chronos in ATN or RSC.

786 B, Biocytin labeled layer 3 cells (white) and GFP positive axons (green) from the ATN or RSC.

787 Scale bar 10  $\mu$ m.

788 C, Firing pattern of two layer 3 cells receiving inputs from the ATN (*cerulean*) and the RSC

789 (*purple*). Insets show current commands.

790 D, Cluster analysis of physiological parameters for cells tested by stimulating ATN or RSC

791 fibers.

792 E, Representative EPSCs evoked in layer 3 cells by light stimulation (blue bar) of ATN or RSC

793 inputs. Right, proportion of cells receiving ATN or RSC inputs.

794 F, Average amplitudes of ATN and RSC induced synaptic currents.

795 G, Latency of EPSCs evoked by light-stimulation of ATN (n = 24 cells) or RSC fibers (n = 27

796 cells).

797 H, EPSPs induced in layer 3 cells (single traces) by stimulating ATN or RSC inputs in absence

798 and presence of 1  $\mu$ M TTX and 100  $\mu$ M 4-AP.

799 I, EPSCs induced by stimulating ATN or RSC fibers in the absence and presence of 100  $\mu$ M

800 APV and APV + 10  $\mu$ M NBQX. Holding potential +40 mV.

801 J, Voltage-clamp responses of layer 3 cells to 20 Hz train stimulations of ATN (*left*) and RSC

802 (*right*) inputs. Insets show EPSCs in response to the first two stimuli.

803 K, oEPSC amplitudes for 10 ATN or RSC fiber stimuli at 20 Hz. n = 15 neurons. Short middle

804 line, mean; Min to max and quartiles.

805 L, Paired-pulse ratio (PPR) and 10/1 ratio (ratio between 10<sup>th</sup> and 1<sup>st</sup> event amplitudes) for

806 ATN or RSC inputs. Wilcoxon matched-pairs signed rank test: ATN PPR vs 10/1 \*\*\*\* p <

807 0.0001, RSC PPR vs 10/1 \*\*\* p = 0.0001.

808 M, Current clamp traces showing action potentials and EPSPs evoked by 10 stimuli at 20 Hz.

809 N, Spiking probability during trains of 10 stimuli. ATN, n = 6, RSC, n = 12. Full line, median;

810 short line, mean; Min to max and quartiles. In K and N, \* p < 0.05, \*\* p < 0.01, \*\*\* p < 0.001,

811 \*\*\*\* p < 0.0001 from Friedman's test followed by Dunn's *post-hoc* test.

812 O, oEPSP amplitudes for trains of 5 stimuli at 20 Hz.

813 See also Figure 2—figure supplements 1 and 2.

814

815

816 **Figure 2—figure supplement 1. Table showing the intrinsic electrophysiological**

817 **physiological properties of layer 3 cells tested for responses to stimulating ATN or RSC**

818 **fibers.**

819

820 **Figure 2—figure supplement 2. Comparison of evoked synaptic events in presubicular layer**

821 **3 neurons following photostimulations of ATN or RSC axons.**

822 A, Variance of latency (jitter) in oEPSP onset following Chronos-expressing ATN or RSC fiber

823 stimuli. RSC input stimulation gives similar variation in latency as ATN inputs.

824 B, Jitter as a function of latency for ATN and RSC stimuli shows a similar coefficient of  
825 variation.  
826 C, Decay time constants of EPSCs evoked in layer 3 neurons by stimulating ATN or RSC inputs.  
827 D, E, First oEPSC amplitude as a function of oEPSC half-width (D) and oEPSC rise time (E) for  
828 both inputs. We found no clear segregation of oEPSC shapes according to the origin of  
829 afferent fibers.  
830 F, oEPSPs in a presubicular layer 3 cell, induced by blue or red light stimulation of Chronos-  
831 expressing ATN or Chrimson-expressing RSC afferents, respectively.  
832 G-J, Comparison of oEPSPs evoked by stimulating ATN or RSC axons, recorded from a same  
833 postsynaptic layer 3 presubicular neuron. G, Mean amplitude. H, Maximum rising slope of  
834 oEPSPs. I, oEPSPs rise time.  $p < 0.05$ , Wilcoxon test. J, oEPSPs decay time constants. oEPSPs  
835 following ATN and RSC fiber stimulation recorded from the same cell are connected by lines.  
836 Dashed lines indicate reversed experimental design (expressing Chronos in RSC and  
837 Chrimson in ATN).  
838 K, Responses to 10 light stimuli at 20 Hz for ATN and RSC inputs to the same cell.  
839 L, Amplitudes of oEPSPs evoked by trains of ATN (left) or RSC (right) fiber stimuli for 11 cells.  
840 Dashed lines indicate the reversed experimental design (expressing Chronos in RSC and  
841 Chrimson in ATN).  
842 M, Summary data from L. On average, the amplitudes of oEPSPs evoked by ATN fiber  
843 stimulation were smaller for the fifth than for the first stimulus. oEPSPs evoked by RSC fiber  
844 stimulation were similar across five stimuli. Full line, median; Short line, mean; Min to max  
845 and quartiles. \*  $p < 0.05$ , Friedman's test and post-hoc Dunn's test comparing each stimulus  
846 with the first.

847  
848

849 **Figure 3** with 1 supplement.

850 **ATN and RSC axons converge in dorsal presubiculum and contact single layer 3 pyramidal**  
851 **neurons.**

852 A, Expression of the blue light sensitive opsin Chronos in ATN and the red light sensitive  
853 opsin Chrimson in RSC.  
854 B, Axons from ATN (GFP labeled, green) and RSC (tdTomato labeled, red) overlap in layer 1  
855 and 3 of dorsal presubiculum. Layer 2 possesses patches of axon-dense and axon-poor  
856 zones. RSC fibers avoid axon-dense microstructures formed by ATN fibers in upper layer 3.  
857 Scale bar, 200  $\mu\text{m}$ .  
858 C, Independent dual wavelength optogenetic stimulation of light sensitive afferent fibers in  
859 presubicular slices.  
860 D, Two biocytin labeled PrS layer 3 pyramidal cells surrounded by ATN (green) and RSC (red)  
861 axons.  
862 E, Patch clamp recording from a layer 3 neuron shows optical EPSCs following  
863 photostimulation of ATN axons (blue light) and RSC axons (red light).  
864 F, 76% of layer 3 pyramidal neurons tested ( $n = 17$ ) received both ATN and RSC input.  
865 G, Distributions of putative synaptic contacts from ATN (green) and RSC (red) on the  
866 dendrites of three layer 3 neurons. Scale bar 50  $\mu\text{m}$ . The boxed area on Cell 2 is shown in  
867 panel I.  
868 H, Normalized number of green and red spots for 6 neurons as a function of the distance  
869 from soma. Paired values are indicated by dotted lines for the 3 cells in G.

870 I, Examples of ATN-labeled (left), RSC-labeled (middle) and both (right) synapses closely  
871 apposed to dendrites of a biocytin-filled layer 3 pyramidal cell. Scale bar 20  $\mu\text{m}$ . Insets show  
872 representative high-magnification images. Scale bar 2  $\mu\text{m}$ .  
873 See also Figure 3—figure supplement 1.

874

875 **Figure 3—figure supplement 1. Calibration of blue and red light stimulation of Chronos and**  
876 **Chrimson.**

877 A, Blue light stimulation of ATN Chronos-expressing fibers evoked oEPSPs in presubicular  
878 layer 3 neurons at an intensity of 0.25mW, and 0.5 ms duration of illumination.

879 B, Blue light stimulation at the same intensity and duration did not evoke oEPSPs from RSC  
880 Chrimson-expressing fibers.

881 C, D, Response probabilities of presubicular layer 3 cells to stimulation of fibers expressing  
882 Chronos or Chrimson with red (C) or blue (D, left) light.

883 E, Experimental design. Injection of AAV5-Chronos-GFP (green) in the ATN, followed by  
884 photostimulation combined with patch recording from a presubicular layer 3 cell.

885 F, Amplitudes of oEPSCs evoked in layer 3 cells by blue (0.5 ms, 0.25 mW) or red light (2 ms,  
886 0.6 mW) stimuli.

887 G, Representative responses to light stimulation of ATN inputs.

888 H, Injection of AAV5-Chrimson-tdTomato (red) in the RSC, followed by photostimulation  
889 combined with patch recording from a presubicular layer 3 cell.

890 I, Amplitudes of oEPSCs evoked in layer 3 cells by blue (0.5 ms, 0.25 mW) or red light (2 ms,  
891 0.6 mW) stimuli.

892 J, Representative responses to light stimulation of RSC inputs

893 K, Values and statistical analysis for different stimulation configurations (Panels F and I).

894

895 **Figure 4. Supralinear summation of EPSPs and action potential firing following**  
896 **photostimulation of ATN and RSC axons.**

897 A, Optical EPSPs in layer 3 neurons in response to blue light activation of ATN axons  
898 (cerulean traces), red light activation of RSC axons (purple traces). Supralinear summation of  
899 EPSPs following coincident activation of both ATN and RSC axons (black traces). The pink  
900 broken line indicates the calculated linear sum of oEPSPs evoked by stimulation of either  
901 ATN or RSC axons. Records from cell 1, Fig 3D.

902 B, Amplitudes of dual ATN and RSC oEPSPs plotted as a function of the sum of separate ATN  
903 and RSC stimulations (*left*). Each circle is a cell (n=11), Pink line ( $\pm 10\%$ ) indicates linearity.  
904 Pie charts give the number of tested layer 3 neurons with supralinear (grey), linear (pink) or  
905 sublinear (white) summation. oEPSPs normalized to linear sum (*bottom right*). Solid circle,  
906 Chronos in ATN/Chrimson in RSC, empty circle, Chronos in RSC/Chrimson in ATN. \*  $p < 0.05$ ,  
907 \*\*  $p < 0.01$ , from Wilcoxon test.

908 C, As in B, for dual ATN and RSC oEPSP integrals.

909 D, oEPSPs induced by 20 Hz stimulation of ATN (cerulean), RSC (purple) or both (black). The  
910 pink broken line indicates the calculated linear sum of oEPSPs evoked by separate ATN and  
911 RSC photostimulation.

912 E, Amplitudes of dual oEPSPs compared to those of the sum of ATN and RSC oEPSPs show  
913 that supralinearity increases across 5 stimulations. Two-way ANOVA,  $p = 0.0117$ . \*  $p < 0.05$ ,  
914 \*\*\*\*  $p < 0.0001$ , Šidák's multiple comparison test. #  $p < 0.05$ , ##  $p < 0.01$ , Friedman's and  
915 *post-hoc* Dunn's test.



916 F, As in E, for dual ATN and RSC oEPSP integrals. Two-way ANOVA,  $p = 0.0128$ .  
917 G, Excitatory postsynaptic responses to photostimulation of ATN (blue light, cerulean traces)  
918 or RSC axons (red light, purple traces) or both (blue and red light, black traces) at resting  
919 membrane potential (-65 mV) or at a depolarized holding potential (-55 mV). Synaptic  
920 excitation led to action potentials when dual ATN and RSC stimuli reached firing threshold.  
921 H, Action potential (AP) probability for either or both stimuli at -65 and -55 mV. Data are  
922 presented as mean  $\pm$  SEM.  
923 I, Action potentials were induced in presubicular layer 3 neurons by near coincident  
924 activation of ATN axons (red light) and RSC axons (blue light). Time delays varied from -50 to  
925 +50 ms.  
926 J, Firing probability was maximal for short delays between -2 to +5 ms (RSC preceding ATN).

927  
928 **Figure 5. EPSP amplifications in layer 3 pyramidal neurons.**

929 A, Optical EPSPs evoked in layer 3 pyramidal neurons following the stimulation of ATN axons  
930 (blue light, cerulean traces), RSC axons (red light, purple traces) or both (blue and red light,  
931 black traces). Recording pipette contained a cesium gluconate based internal solution and  
932 the Na<sup>+</sup> channel blocker QX-314. A large all-or-none EPSP amplification occurred for dual  
933 stimuli at 20 Hz, on some trials.  
934 B, In the presence of the GABA<sub>A</sub> receptor antagonist gabazine (10  $\mu$ M), dual EPSP  
935 amplification occurred earlier in the train.  
936 C, The additional presence of the NMDA receptor antagonist APV (100  $\mu$ M) abolished dual  
937 EPSP amplification (black trace). EPSP amplification was partially restored by increasing red  
938 light intensity x2 (pale pink traces).

939

940 **Figure 6 with 2 supplements.**

941 **Presubicular LMN-projecting layer 4 neurons avoid thalamo-recipient layer 3 and receive**  
942 **little direct input from ATN and RSC.**

943 A, Expression of Chronos-GFP in ATN and retrograde labeling of neurons that target LMN.  
944 B, Thalamic axons (green) in superficial layers 1 and 3 of presubiculum. Retrobeads label cell  
945 bodies of presubicular layer 4 cells (red).  
946 C, Retrograde rAAV2-tdTomato label cell bodies and dendrites of layer 4 LMN projecting  
947 neurons (red). Apical dendrites of layer 4 pyramidal neurons avoid layer 3 where thalamic  
948 axons ramify.  
949 D, Presubicular slice containing two layer 3 and two layer 4 neurons filled with biocytin  
950 (white) and GFP expressing thalamic axons (green). Scale bar 100  $\mu$ m. Inset, retrobeads (red)  
951 in the soma of a biocytin filled LMN-projecting layer 4 neuron. Scale bar 10  $\mu$ m.  
952 E, Layer 3 neurons are regular spiking and layer 4 neurons are burst firing, initially and at  
953 rebound, in response to current injection. Black trace, rheobase.  
954 F, T-type Ca<sup>2+</sup> channel blocker TTA-P2 (1  $\mu$ M) suppressed burst firing in presubicular layer 4  
955 neurons, while single action potentials were preserved.  
956 G. Representative oEPSCs in layer 3 (left) and layer 4 (right) pyramidal cells, in response to  
957 stimulation of ATN (cerulean) or RSC (purple) inputs.  
958 H, oEPSC latencies in layer 3 and layer 4 cells, for ATN inputs (left, cerulean), or RSC inputs  
959 (right, purple). Each dot is a cell. Same layer 4 cells are indicated by connecting lines, to  
960 show the difference in latency for direct and indirect synaptic responses.  
961 I, oEPSPs in layer 4 neurons in response to stimulation of ATN (cerulean) or RSC (purple)  
962 inputs in control and in the presence of TTX (1  $\mu$ M) and 4-AP (100  $\mu$ M). Dashed lines indicate

963 the timing of the large disynaptic component of the responses (i, indirect), and the small  
964 monosynaptic response (d, direct), isolated in TTX-4AP.  
965 See also Figure 6—figure supplements 1 and 2.

966  
967

968 **Figure 6—figure supplement 1. Apical dendrites of presubicular layer 4 neurons avoid the**  
969 **thalamorecipient layer 3.**

970 A, Retrograde AAV2retro-tdTom was injected in LMN.  
971 B, PrS L4 neuron cell bodies and dendrites were labeled. Scale bar, 50  $\mu\text{m}$ . Full arrowheads,  
972 L4 neurons apical dendrites crossing L3; Empty arrowheads, L4 neurons apical dendrites  
973 skirting L3.  
974 C, Anterograde AAV5-Chronos-GFP was injected in ATN to label thalamic axons, delimiting  
975 PrS layer 3.  
976 D, Examples of biocytin filled layer 4 presubicular neurons. (1) The apical dendrite of this  
977 neuron avoided the densely packed ATN afferents and it didn't show responses to thalamic  
978 stimulations. (2) This neuron's apical dendrite crossed trough a short stretch of layer 3  
979 containing ATN afferents, and it responded with low amplitude indirect events. (3) The apical  
980 dendrite of this neuron crossed layer 3 and the zone containing ATN afferents, and was  
981 directly recruited. Scale bar 10 $\mu\text{m}$ .  
982 E, AAV-Chronos-GFP injected in ATN, and AAV-Chrimson-tdTom injected in RSC.  
983 F, Image from Figure 7 panel D. Scale bar 100 $\mu\text{m}$ .  
984 G, (Left) Enlarged view of dotted area in A, with two labelled L4 neurons. The apical dendrite  
985 of top neuron makes a U-turn to ramify in deep layers and seems to cross path with the axon  
986 of the bottom neuron, potentially forming a synaptic contact. (Right) The dendrite of the top  
987 neuron and axon of bottom neuron are overlayed with pink and green lines respectively.  
988 Scale bar 20 $\mu\text{m}$ .

989

990 **Figure 6—figure supplement 2. Electrophysiological passive and active intrinsic properties**  
991 **of layer 3 vs. layer 4 neurons.**

992 Data for layer 3 are summarized in Figure 2—figure supplement 1 and are shown here for  
993 comparison. Statistical differences are indicated as levels of p values (\*  $p < 0.05$ , \*\*  $p < 0.01$ ,  
994 \*\*\*  $p < 0.001$ , \*\*\*\*  $p < 0.0001$ ) obtained from Mann-Whitney tests between layer 4 ( $n = 19$ )  
995 and layer 3 ( $n = 33$ ) for each parameter. Box plots indicate maximum and minimum values,  
996 quartiles, full line is the median, short line is the mean.

997

998 **Figure 7** with 1 supplement.

999 **Cross-laminar activation of LMN-projecting layer 4 bursting neurons.**

1000 A, Simultaneous records of a layer 4 and a layer 3 neuron during photostimulation of ATN  
1001 afferents. EPSP onset was delayed in the layer 4 neuron. Right panel, expanded view of the  
1002 boxed area.  
1003 B, Simultaneous records of a layer 4 and a layer 3 neuron during photostimulation of RSC  
1004 afferents. As in A, layer 4 neurons responded with a delay. Right panel, expanded view of the  
1005 boxed area.  
1006 C, Latencies of synaptic activation indicated by the dotted lines in A, B (ATN stimulation,  $n = 4$   
1007 cells; RSC stimulation,  $n = 1$ ). EPSP onset and AP peak from layer 3 neurons ( $n = 5$ ). Dotted  
1008 lines link to the EPSP onset in simultaneously recorded layer 4 neurons ( $n = 5$ ).  $p < 0.05$ ,  
1009 Kruskal-Wallis multiple comparison test.

1010 D, Biocytin labeled layer 3 and layer 4 pyramidal neurons, in a presubicular slice containing  
1011 thalamic (green) and retrosplenial (red) axons. The apical dendrite of one layer 4 neuron  
1012 makes a U-turn (arrowhead), away from layer 3, where the thalamic axons ramify. The  
1013 neighboring layer 4 neuron's apical dendrite crosses the thalamo-recipient layer 3 for a short  
1014 distance before arborizing outside of ATN targeted area, towards the subiculum, on the  
1015 right. Another biocytin filled layer 4 neuron's dendrites extend toward the deep layers. Scale  
1016 bar, 100 $\mu$ m.

1017 E, Simultaneous records from a layer 3 and a layer 4 cell to ATN input stimulation (top, 0.25  
1018 mW, blue light), ATN and RSC input stimulation (middle, 0.25 mW blue and 0.25 mW red  
1019 light; light intensities compatible with independent photostimulation) or non-specific ATN  
1020 and RSC input stimulation (bottom, 3.25 mW blue and 0.25 mW red light). ATN fibers  
1021 expressed Chronos-GFP (green) and RSC fibers expressed Chrimson-tdTomato (red).

1022 F, Top, oEPSPs and bursts of action potentials in a layer 4 neuron, evoked by dual wavelength  
1023 stimulation of ATN and RSC afferents at 20 Hz. Amplifications of dual oEPSPs led to firing.  
1024 Bottom, the NMDA receptor antagonist APV (100  $\mu$ M) reduced EPSP amplification and  
1025 prevented action potential firing.

1026 G. Layer 4 bursting neurons are sensitive to the acetylcholine receptor agonist carbachol (10  
1027  $\mu$ M). Action potential firing in response to step current injections in control (black), in the  
1028 presence of carbachol (grey), and after wash-out (black). Bottom graph, membrane  
1029 potential depolarization during a 2-minute carbachol application. The number of action  
1030 potentials increased during the depolarizing steps (i) and on the baseline (ii).

1031 See also Figure 7—figure supplement 1.

1032

1033

1034 **Figure 7—figure supplement 1. Regular firing layer 3 vs. intrinsically bursting layer 4**  
1035 **neurons responded to high-intensity light stimulations of ATN or RSC afferents.**

1036 Layer 3 neurons respond with single spikes following each light stimulation while layer 4  
1037 neurons respond with bursts of action potentials at the beginning of the stimulation train.

1038

## 1039 **References**

1040

1041 Alexander AS, Nitz DA. 2015. Retrosplenial cortex maps the conjunction of internal and  
1042 external spaces. *Nat Neurosci* 18:1143–1151.

1043 Auger SD, Mullally SL, Maguire EA. 2012. Retrosplenial Cortex Codes for Permanent  
1044 Landmarks. *PLOS ONE* 7:e43620.

1045 Balsamo G, Blanco-Hernández E, Liang F, Naumann RK, Coletta S, Burgalossi A, Preston-  
1046 Ferrer P. 2022. Modular microcircuit organization of the presubicular head-direction  
1047 map. *Cell Rep* 39, 110684.

1048 Blair HT, Sharp PE. 1995. Anticipatory head direction signals in anterior thalamus: evidence  
1049 for a thalamocortical circuit that integrates angular head motion to compute head  
1050 direction. *J Neurosci* 15:6260–6270.

1051 Boccara CN, Sargolini F, Thoresen VH, Solstad T, Witter MP, Moser EI, Moser M-B. 2010. Grid  
1052 cells in pre- and parasubiculum. *Nat Neurosci* 13:987–994.

1053 Boehm J, Kang M-G, Johnson RC, Esteban J, Huganir RL, Malinow R. 2006. Synaptic  
1054 incorporation of AMPA receptors during LTP is controlled by a PKC phosphorylation

1055 site on GluR1. *Neuron*. 51:213–225.

1056 Calton JL, Stackman RW, Goodridge JP, Archey WB, Dudchenko PA, Taube JS. 2003.  
 1057 Hippocampal place cell instability after lesions of the head direction cell network. *J*  
 1058 *Neurosci* 23:9719–9731.

1059 Clark BJ, Bassett JP, Wang SS, Taube JS. 2010. Impaired Head Direction Cell Representation in  
 1060 the Anterodorsal Thalamus after Lesions of the Retrosplenial Cortex. *J Neurosci*  
 1061 30:5289–5302.

1062 Fallahnezhad M, Le Mero J, Zenelaj X, Vincent J, Rochefort C, Rondi-Reig L. 2023. Cerebellar  
 1063 control of a unitary head direction sense. *Proc Natl Acad Sci U S A* 120:e2214539120.

1064 Fisher YE, Marquis M, D’Alessandro I, Wilson RI. 2022. Dopamine promotes head direction  
 1065 plasticity during orienting movements. *Nature* 612:316–322.

1066 Fricker D, Miles R. 2000. EPSP amplification and the precision of spike timing in hippocampal  
 1067 neurons. *Neuron*. 28:559–569.

1068 Fricker D, Dinocourt C, Eugène E, Wood JN, Wood J, Miles R. 2009. Pyramidal cells of rodent  
 1069 presubiculum express a tetrodotoxin-insensitive Na<sup>+</sup> current. *J Physiol* 587:4249–  
 1070 4264.

1071 Gil Z, Connors BW, Amitai Y. 1999. Efficacy of thalamocortical and intracortical synaptic  
 1072 connections: quanta, innervation, and reliability. *Neuron* 23:385–397.

1073 Goodridge JP, Taube JS. 1997. Interaction between the postsubiculum and anterior thalamus  
 1074 in the generation of head direction cell activity. *J Neurosci* 17:9315–9330.

1075 Häusser M, Mel B. 2003. Dendrites: bug or feature? *Current Opinion in Neurobiology*.  
 1076 13:372–383.

1077 Hedrick NG, Lu Z, Bushong E, Singhi S, Nguyen P, Magaña Y, Jilani S, Lim BK, Ellisman M,  
 1078 Komiyama T. 2022. Learning binds new inputs into functional synaptic clusters via  
 1079 spinogenesis. *Nat Neurosci* 25:726–737.

1080 Hooks BM, Lin JY, Guo C, Svoboda K. 2015. Dual-channel circuit mapping reveals  
 1081 sensorimotor convergence in the primary motor cortex. *Journal of Neuroscience*.  
 1082 35:4418–4426.

1083 Huang L-W, Simonnet J, Nassar M, Richevaux L, Lofredi R, Fricker D. 2017. Laminar  
 1084 Localization and Projection-Specific Properties of Presubicular Neurons Targeting the  
 1085 Lateral Mammillary Nucleus, Thalamus, or Medial Entorhinal Cortex. *eneuro*  
 1086 4:ENEURO.0370-16.2017.

1087 Ishihara Y, Fukuda T. 2016. Immunohistochemical investigation of the internal structure of  
 1088 the mouse subiculum. *NSC*. 337:1–25.

1089 Jacob P-Y, Casali G, Spieser L, Page H, Overington D, Jeffery K. 2017. An independent,  
 1090 landmark-dominated head-direction signal in dysgranular retrosplenial cortex. *Nat*  
 1091 *Neurosci* 20:173–175.

1092 Jeffery KJ, Page HJ, Stringer SM. 2016. Optimal cue combination and landmark-stability  
 1093 learning in the head direction system. *J Physiol. Lond*). 594:6527–6534.

1094 Jones BF, Witter MP. 2007. Cingulate cortex projections to the parahippocampal region and  
 1095 hippocampal formation in the rat. *Hippocampus* 17:957–976.

1096 Keshavarzi S, Bracey EF, Faville RA, Campagner D, Tyson AL, Lenzi SC, Branco T, Margrie TW.  
 1097 2022. Multisensory coding of angular head velocity in the retrosplenial cortex.

1098 Neuron 110:532-543.e9.

1099 Klapoetke NC et al. 2014. Independent optical excitation of distinct neural populations. *Nat*  
1100 *Methods* 11:338–346.

1101 Knierim JJ, Zhang K. 2012. Attractor dynamics of spatially correlated neural activity in the  
1102 limbic system. *Annu Rev Neurosci* 35:267–285.

1103 Kononenko NL, Witter MP. 2012. Presubiculum layer III conveys retrosplenial input to the  
1104 medial entorhinal cortex. *Hippocampus* 22:881–895.

1105 Larkum ME, Zhu JJ, Sakmann B. 1999. A new cellular mechanism for coupling inputs arriving  
1106 at different cortical layers. *Nature* 398, 338–341.

1107 Larkum ME, Waters J, Sakmann B, Helmchen F. 2007. Dendritic spikes in apical dendrites of  
1108 neocortical layer 2/3 pyramidal neurons. *J. Neurosci.* 27, 8999–9008.

1109 Larkum ME, Nevian T, Sandler M, Polsky A, Schiller J. 2009. Synaptic Integration in Tuft  
1110 Dendrites of Layer 5 Pyramidal Neurons: A New Unifying Principle. *Science* 325, 756–  
1111 760.

1112 Lavzin M, Rapoport S, Polsky A, Garion L, Schiller J. 2012. Nonlinear dendritic processing  
1113 determines angular tuning of barrel cortex neurons in vivo. *Nature.* 490:397–401.

1114 Liu J, Kashima T, Morikawa S, Noguchi A, Ikegaya Y, Matsumoto N. 2021. Molecular  
1115 characterization of superficial layers of the presubiculum during development. *Front*  
1116 *Neuroanat* 15.

1117 Makarov R, Pagkalos M, Poirazi P. 2023. Dendrites and Efficiency: Optimizing Performance  
1118 and Resource Utilization. <https://arxiv.org/abs/2306.07101>.

1119 Martin LJ, Blackstone CD, Levey AI, Huganir RL, Price DL. 1993. AMPA glutamate receptor  
1120 subunits are differentially distributed in rat brain. *NSC.* 53:327–358.

1121 Mathon B, Nassar M, Simonnet J, Le Duigou C, Clemenceau S, Miles R, Fricker D. 2015.  
1122 Increasing the effectiveness of intracerebral injections in adult and neonatal mice: a  
1123 neurosurgical point of view. *Neurosci Bull* 31:685–696.

1124 McNaughton BL, Battaglia FP, Jensen O, Moser EI, Moser M-B. 2006. Path integration and the  
1125 neural basis of the “cognitive map.” *Nat Rev Neurosci* 7:663–678.

1126 Mel BW. Synaptic integration in an excitable dendritic tree. 1993. *J Neurophysiol.* 70(3):1086-  
1127 101.

1128 Milstein AD, Bloss EB, Apostolides PF, Vaidya SP, Dilly GA, Zemelman BV, Magee JC. 2015.  
1129 Inhibitory Gating of Input Comparison in the CA1 Microcircuit. *Neuron* 87:1274–  
1130 1289.

1131 Mitchell AS, Czajkowski R, Zhang N, Jeffery KJ, Nelson AJD. 2018. Retrosplenial cortex and its  
1132 role in spatial cognition. *Brain and Neuroscience Advances.* 8:586.

1133 Nassar M, Simonnet J, Huang L-W, Mathon B, Cohen I, Bendels MHK, Beranek M, Miles R,  
1134 Fricker D. 2018. Anterior Thalamic Excitation and Feedforward Inhibition of  
1135 Presubicular Neurons Projecting to Medial Entorhinal Cortex. *J Neurosci* 38:6411–  
1136 6425.

1137 Naud R, Friedenberger Z, Toth K. 2023. Silences, Spikes and Bursts: Three-Part Knot of the  
1138 Neural Code. *arXiv:2302.07206v1.* 1–15.

1139 Payeur A, Guerguiev J, Zenke F, Richards BA, Naud R. 2021. Burst-dependent synaptic

1140           plasticity can coordinate learning in hierarchical circuits. *Nat Neurosci* 24:1010–1019.

1141 Peng Y, Barreda Tomás FJ, Klisch C, Vida I, Geiger JRP. 2017. Layer-Specific Organization of  
1142 Local Excitatory and Inhibitory Synaptic Connectivity in the Rat Presubiculum. *Cereb*  
1143 *Cortex*. 27:2435-2452.

1144 Peyrache A, Lacroix MM, Petersen PC, Buzsáki G. 2015. Internally organized mechanisms of  
1145 the head direction sense. *Nat Neurosci* 18:569–575.

1146 Poirazi P, Brannon T, Mel BW. 2003. Arithmetic of subthreshold synaptic summation in a  
1147 model CA1 pyramidal cell. *Neuron*. 37(6):977-87.

1148 Poirazi P, Papoutsi A. 2020. Illuminating dendritic function with computational models. *Nat*  
1149 *Rev Neurosci* 1–19.

1150 Polsky A, Mel BW, Schiller J. 2004. Computational subunits in thin dendrites of pyramidal  
1151 cells. *Nat Neurosci* 7:621–627.

1152 Porter JT, Cauli B, Tsuzuki K, Lambolez B, Rossier J, Audinat E. 1999. Selective excitation of  
1153 subtypes of neocortical interneurons by nicotinic receptors. *J Neurosci* 19:5228–  
1154 5235.

1155 Preston-Ferrer P, Coletta S, Frey M, Burgalossi A. 2016. Anatomical organization of  
1156 presubicular head-direction circuits. *eLife* 5.

1157 Ranck JB. 1984. Head direction cells in the deep layer of dorsal presubiculum in freely  
1158 moving rats. *Soc Neurosci Abstr*.

1159 Rees CL, Moradi K, Ascoli GA. 2017. Weighing the Evidence in Peters’ Rule: Does Neuronal  
1160 Morphology Predict Connectivity? *Trends Neurosci* 40:63–71.

1161 Richevaux L, Schenberg L, Beranek M, Fricker D. 2019. In Vivo Intracerebral Stereotaxic  
1162 Injections for Optogenetic Stimulation of Long-Range Inputs in Mouse Brain Slices.  
1163 *JoVE J Vis Exp* e59534.

1164 Shibata H, Honda Y. 2012. Thalamocortical projections of the anterodorsal thalamic nucleus  
1165 in the rabbit. *J Comp Neurol* 520:2647–2656.

1166 Simonnet J, Eugène E, Cohen I, Miles R, Fricker D. 2013. Cellular neuroanatomy of rat  
1167 presubiculum. *Eur J Neurosci* 37:583–597.

1168 Simonnet J, Nassar M, Stella F, Cohen I, Mathon B, Boccara CN, Miles R, Fricker D. 2017.  
1169 Activity dependent feedback inhibition may maintain head direction signals in mouse  
1170 presubiculum. *Nat Commun* 8:16032.

1171 Simonnet J, Richevaux L, Fricker D. 2021. Single or Double Patch-Clamp Recordings In Ex Vivo  
1172 Slice Preparation: Functional Connectivity, Synapse Dynamics, and Optogenetics.  
1173 *Methods Mol Biol Clifton NJ* 2188:285–309.

1174 Sit KK, Goard MJ. 2023. Coregistration of heading to visual cues in retrosplenial cortex. *Nat*  
1175 *Commun* 14:1992.

1176 Skaggs WE, Knierim JJ, Kudrimoti HS, McNaughton BL. 1995. A model of the neural basis of  
1177 the rat’s sense of direction. *Adv Neural Inf Process Syst* 7:173–180.

1178 Slomianka L, Geneser FA. 1991. Distribution of acetylcholinesterase in the hippocampal  
1179 region of the mouse: I. Entorhinal area, parasubiculum, retrosplenial area, and  
1180 presubiculum. *J Comp Neurol* 303:339–354.

1181 Smith SL, Smith IT, Branco T, Häusser M. 2013. Dendritic spikes enhance stimulus selectivity

1182 in cortical neurons in vivo. *Nature*. 503:115–120.

1183 Spruston N. Pyramidal neurons: dendritic structure and synaptic integration. 2008. *Nat Rev*  
1184 *Neurosci*. 9(3):206-21.

1185 Stackman RW, Taube JS. 1998. Firing properties of rat lateral mammillary single units: head  
1186 direction, head pitch, and angular head velocity. *J Neurosci* 18:9020–9037.

1187 Sugar J, Witter MP. 2016. Postnatal development of retrosplenial projections to the  
1188 parahippocampal region of the rat. *eLife* 5.

1189 Takahashi N, Oertner TG, Hegemann P, Larkum ME. 2016. Active cortical dendrites modulate  
1190 perception. *Science* 354:1587–1590.

1191 Takahashi N, Ebner C, Sigl-Glöckner J, Moberg S, Nierwetberg S, Larkum ME. 2020. Active  
1192 dendritic currents gate descending cortical outputs in perception. *Nat Neurosci*.  
1193 54:677–679.

1194 Taube JS. 1995. Head direction cells recorded in the anterior thalamic nuclei of freely moving  
1195 rats. *J Neurosci* 15:70–86.

1196 Taube JS, Muller RU, Ranck JB. 1990a. Head-direction cells recorded from the postsubiculum  
1197 in freely moving rats. I. Description and quantitative analysis. *J Neurosci* 10:420–435.

1198 Taube JS, Muller RU, Ranck JB. 1990b. Head-direction cells recorded from the postsubiculum  
1199 in freely moving rats. II. Effects of environmental manipulations. *J Neurosci* 10:436–  
1200 447.

1201 Tukker JJ, Tang Q, Burgalossi A, Brecht M. 2015. Head-Directional Tuning and Theta  
1202 Modulation of Anatomically Identified Neurons in the Presubiculum. *Journal of*  
1203 *Neuroscience*. 35:15391–15395.

1204 Van der Goes M-SH, Voigts J, Newman JP, Toloza EHS, Brown NJ, Murugan P, Harnett MT.  
1205 2022. Coordinated Head Direction Representations in Mouse Anterodorsal Thalamic  
1206 Nucleus and Retrosplenial Cortex. [bioRxiv doi.org/10.1101/2022.08.20.504604](https://doi.org/10.1101/2022.08.20.504604).

1207 Van Groen T, Wyss JM. 2003. Connections of the retrosplenial granular b cortex in the rat. *J*  
1208 *Comp Neurol* 463:249–263.

1209 Van Groen T, Wyss JM. 1992. Connections of the retrosplenial dysgranular cortex in the rat. *J*  
1210 *Comp Neurol* 315:200–216.

1211 Van Groen T, Wyss JM. 1990a. The connections of presubiculum and parasubiculum in the  
1212 rat. *Brain Res* 518:227–243.

1213 Van Groen T, Wyss JM. 1990b. Connections of the retrosplenial granular a cortex in the rat. *J*  
1214 *Comp Neurol* 300:593–606.

1215 Van Groen T, Wyss JM. 1990c. The postsubicular cortex in the rat: characterization of the  
1216 fourth region of the subicular cortex and its connections. *Brain Res* 529:165–177.

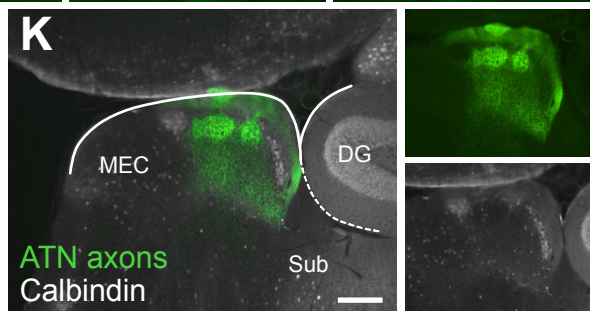
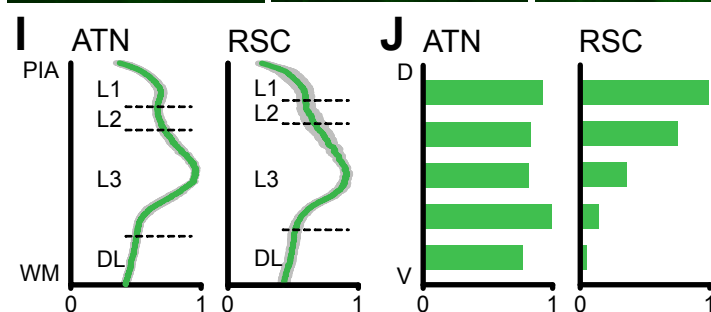
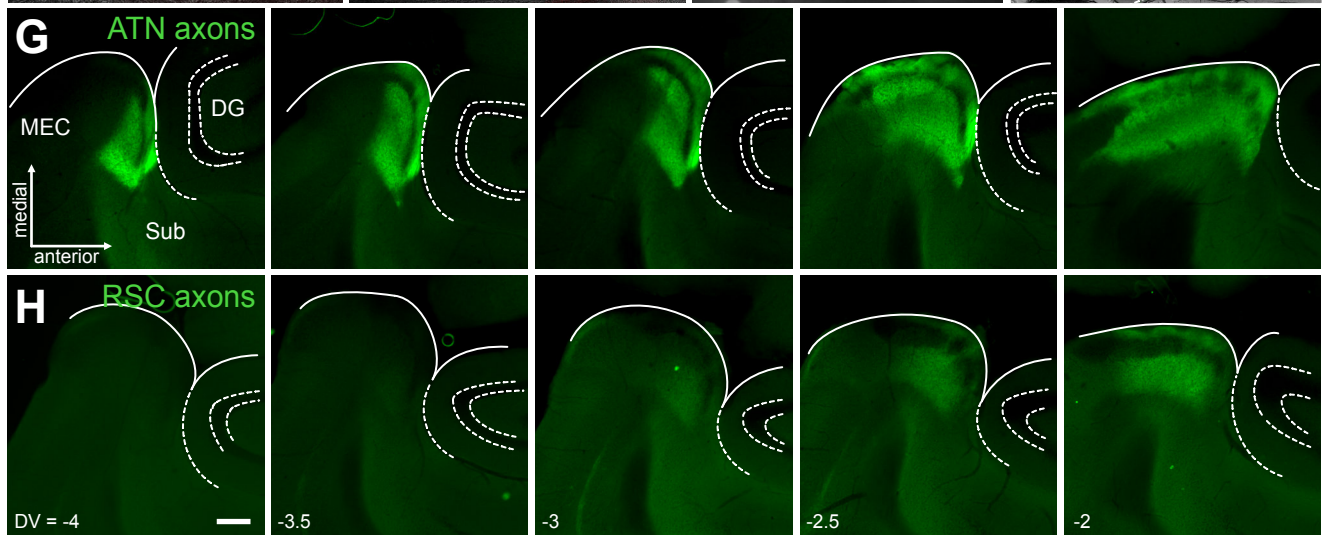
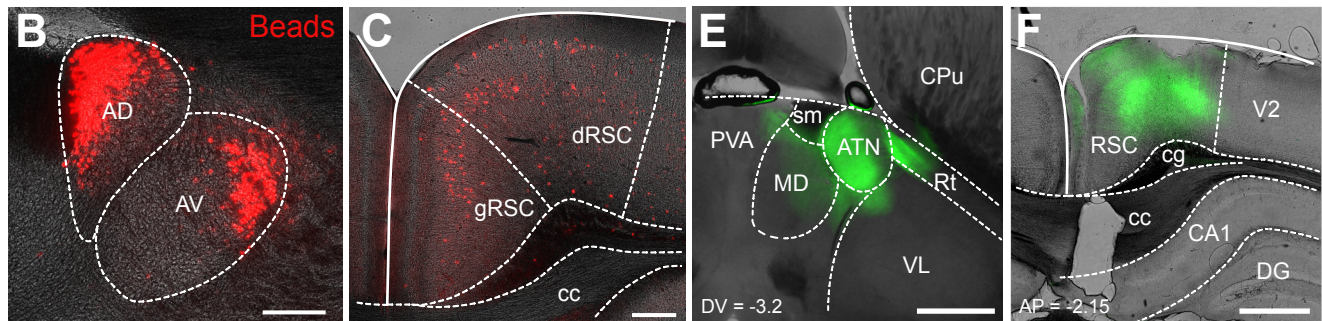
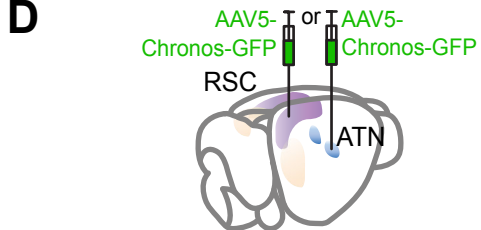
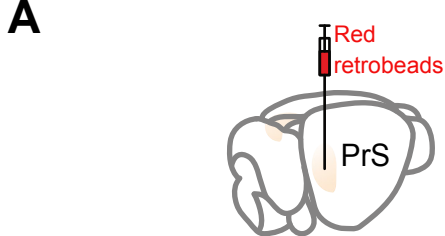
1217 Vann SD, Aggleton JP, Maguire EA. 2009. What does the retrosplenial cortex do? *Nat Rev*  
1218 *Neurosci*. 10:792–802.

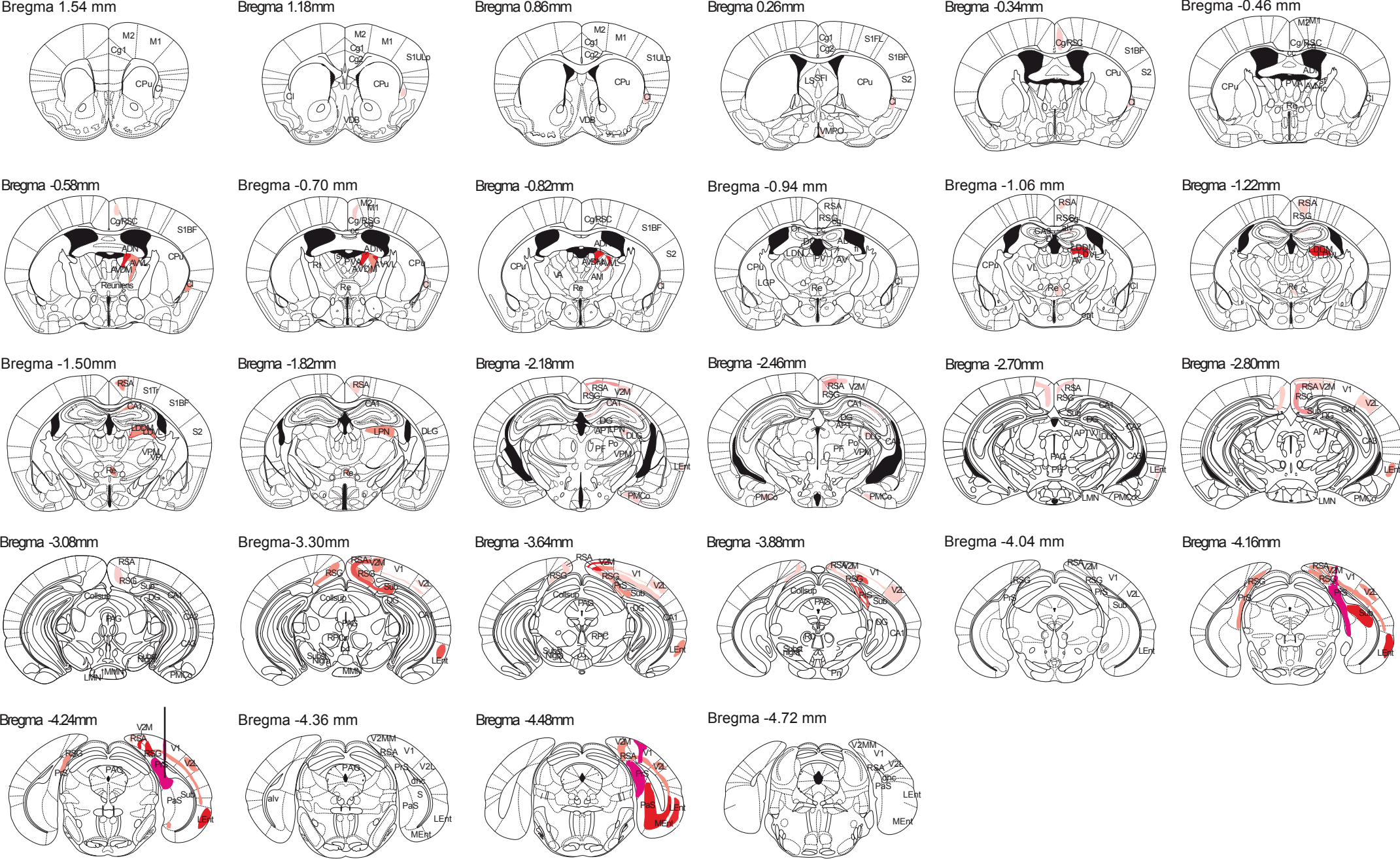
1219 Vogt BA, Miller MW. 1983. Cortical connections between rat cingulate cortex and visual,  
1220 motor, and postsubicular cortices. *J Comp Neurol* 216:192–210.

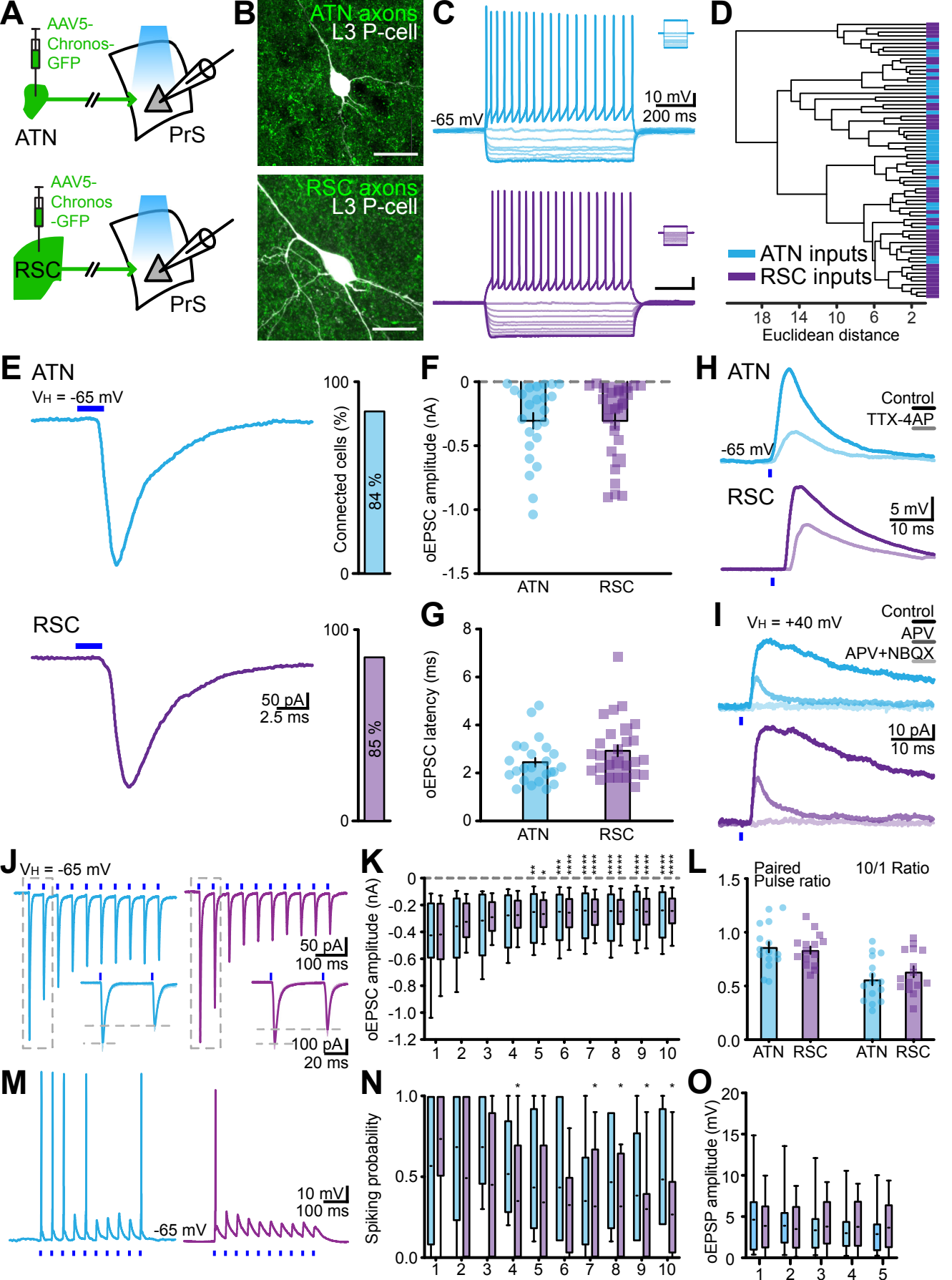
1221 Wilson DE, Whitney DE, Scholl B, Fitzpatrick D. 2016. Orientation selectivity and the  
1222 functional clustering of synaptic inputs in primary visual cortex. *Nat Neurosci*.  
1223 19:1003–1009.

- 1224 Yoder RM, Peck JR, Taube JS. 2015. Visual landmark information gains control of the head  
1225 direction signal at the lateral mammillary nuclei. *J Neurosci* 35:1354–1367.
- 1226 Yoder RM, Taube JS. 2011. Projections to the anterodorsal thalamus and lateral mammillary  
1227 nuclei arise from different cell populations within the postsubiculum: implications for  
1228 the control of head direction cells. *Hippocampus* 21:1062–1073.
- 1229 Yoder RM, Chan JHM, Taube JS. 2017. Acetylcholine Contributes to the Integration of Self-  
1230 Movement Cues in Head Direction Cells. *Behav Neurosci* 131:312-324.
- 1231 Yoder RM, Valerio S, Crego ACG, Clark BJ, Taube JS. 2019. Bilateral postsubiculum lesions  
1232 impair visual and nonvisual homing performance in rats. *Behav Neurosci* 133:496–  
1233 507.
- 1234 Zugaro MB, Arleo A, Berthoz A, Wiener SI. 2003. Rapid spatial reorientation and head  
1235 direction cells. *J Neurosci* 23:3478–3482.
- 1236



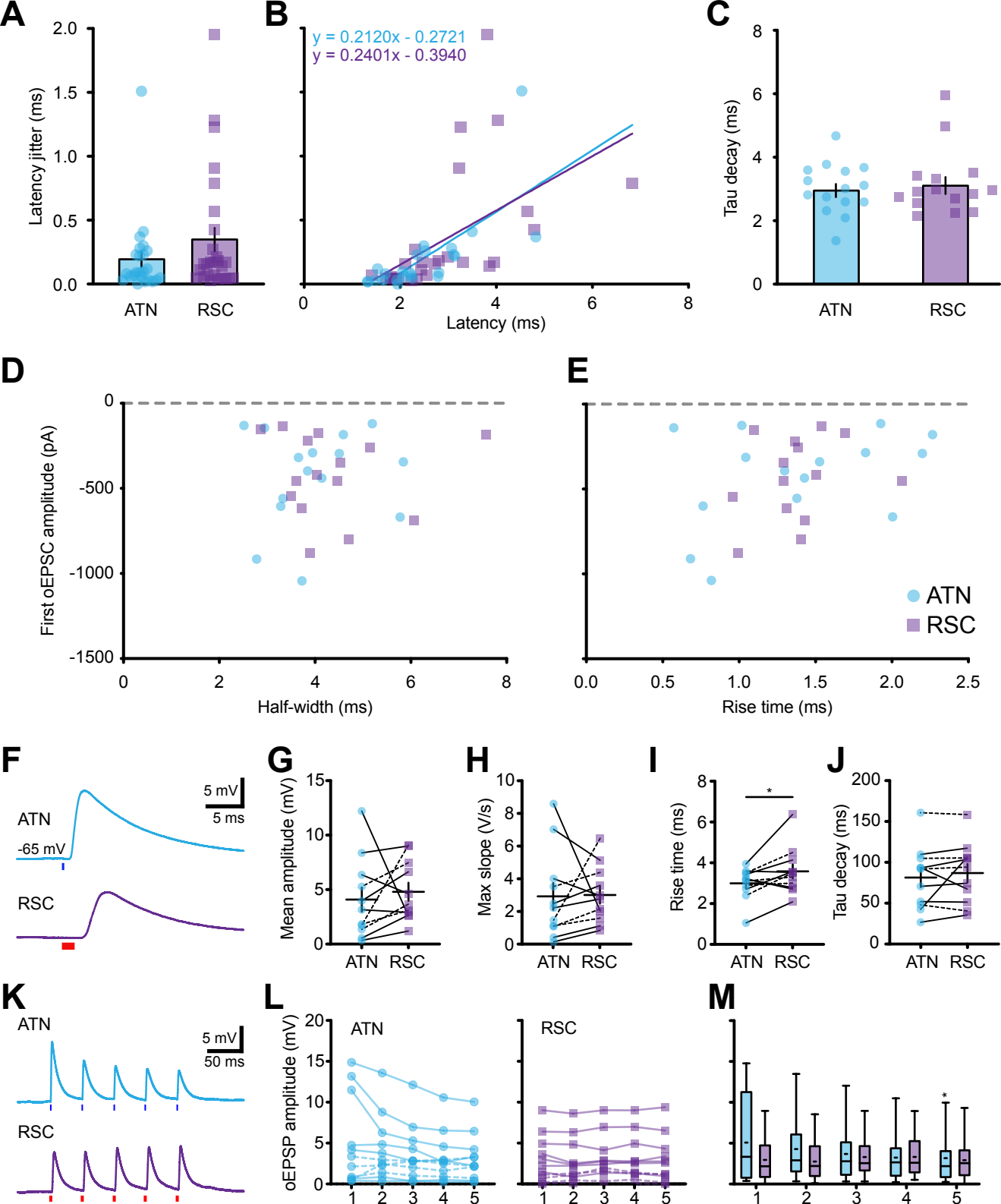


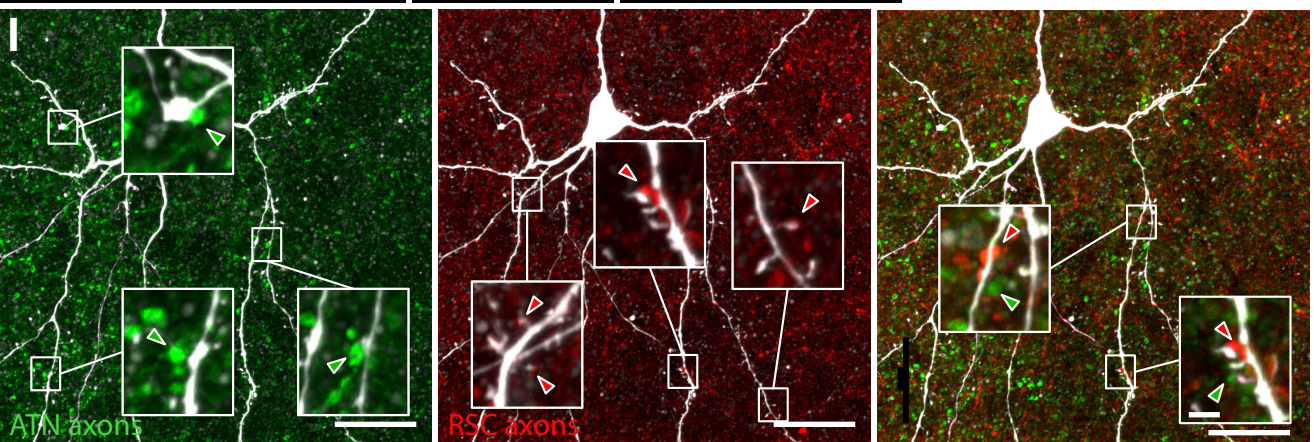
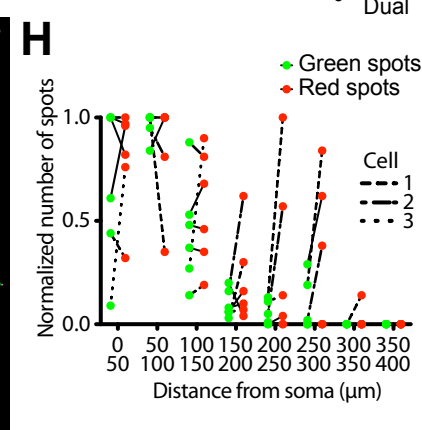
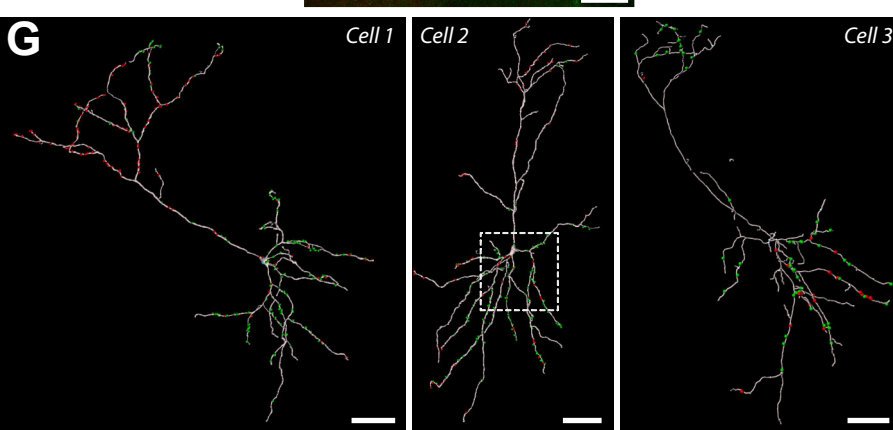
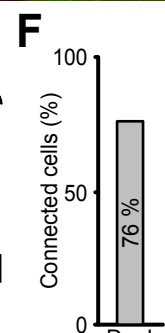
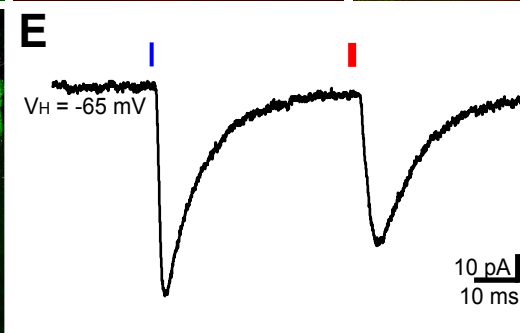
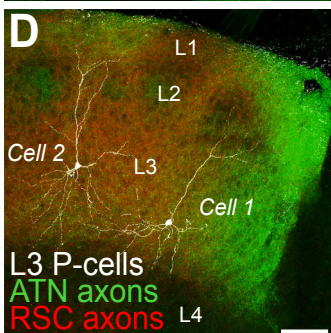
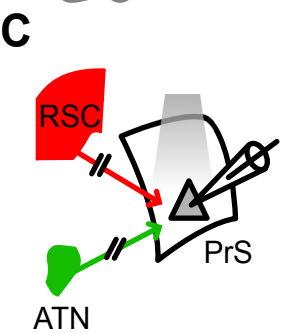
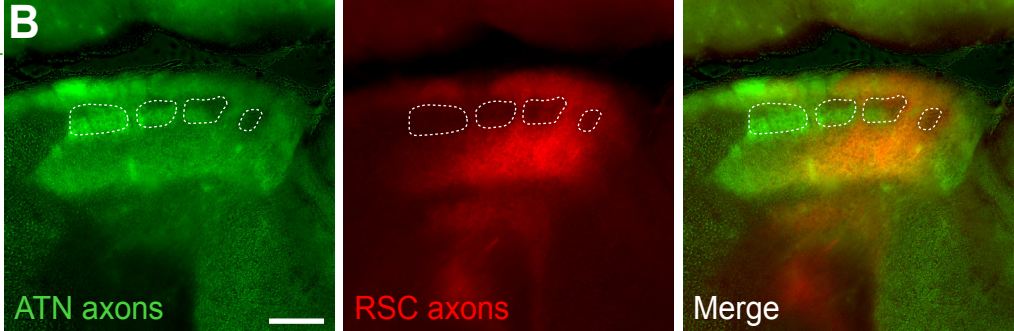
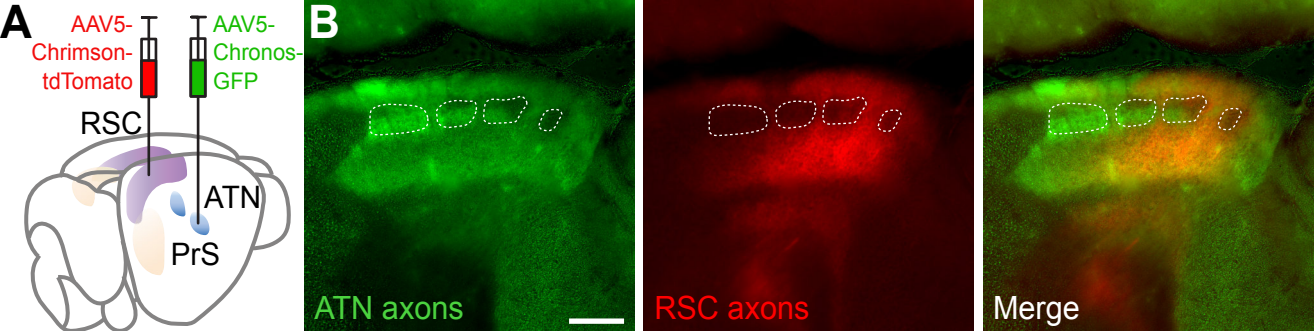


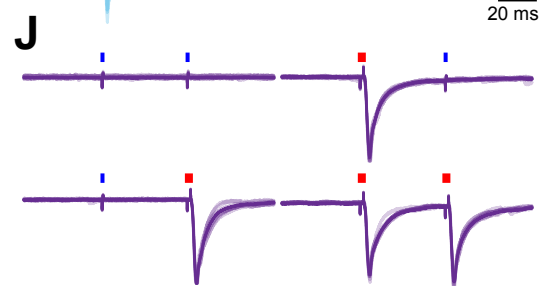
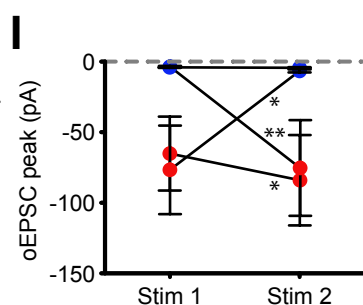
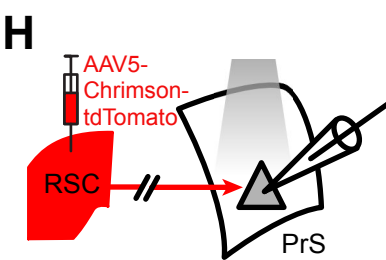
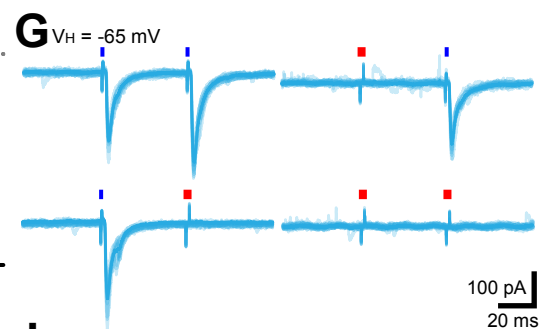
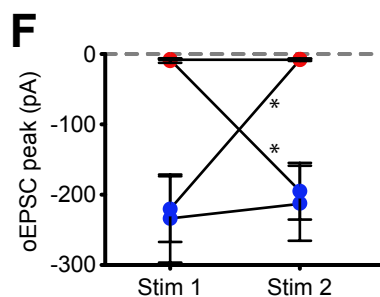
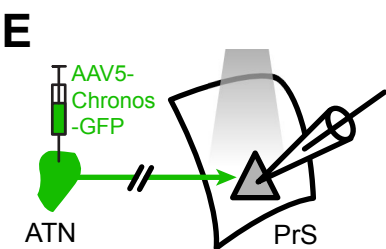
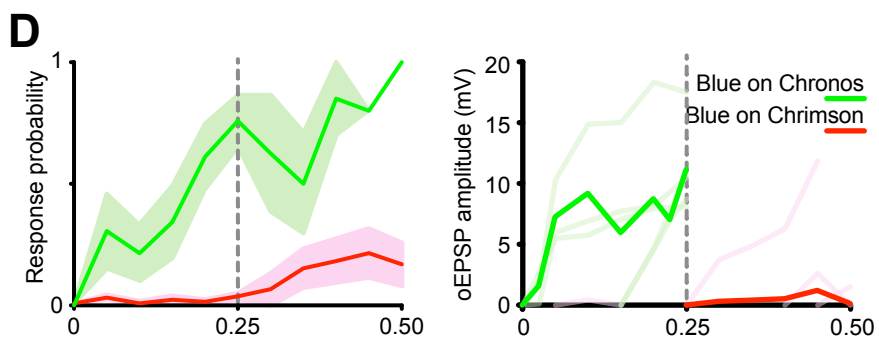
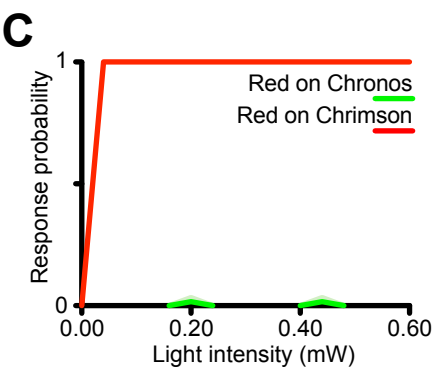
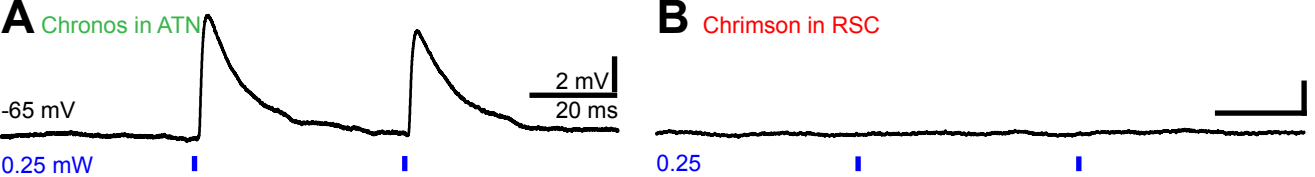


	ATN			RSC			<i>p-value</i>
	Mean	SEM	n	Mean	SEM	n	Mann-Whitney
<b>Resting membrane potential (mV)</b>	-71.37	1.85	27	-73.50	1.52	38	<i>ns</i>
<b>Neuronal input resistance (MΩ)</b>	414.5	31.5	27	349.8	23.4	38	<i>ns</i>
<b>Tau 1 (ms)</b>	26.46	1.80	27	22.25	1.19	38	<i>0.0481</i>
<b>Sag ratio at -100 mV</b>	1.07	0.01	27	1.10	0.01	38	<i>ns</i>
<b>Rheobase current (pA)</b>	51.88	5.25	27	63.00	3.67	38	<i>0.0188</i>
<b>Firing rate at 200 pA (Hz)</b>	39.21	3.87	27	45.10	3.02	38	<i>ns</i>
<b>Maximum firing frequency (Hz)</b>	48.19	4.56	27	64.84	5.02	38	<i>0.0035</i>
<b>Input-output slope (Hz/nA)</b>	357.5	30.0	27	376.7	24.6	38	<i>ns</i>
<b>AP threshold (mV)</b>	-34.13	0.86	27	-33.48	0.91	38	<i>ns</i>
<b>AP width (ms)</b>	0.77	0.06	27	0.68	0.04	38	<i>ns</i>
<b>AP AHP (mV)</b>	-20.25	0.64	27	-18.77	0.47	38	<i>ns</i>
<b>AP rise amplitude (mV)</b>	77.84	1.67	27	79.77	1.26	38	<i>ns</i>
<b>AP maximum depolarization rate (V/s)</b>	323.7	11.0	27	350.7	9.2	38	<i>0.0326</i>
<b>AP maximum repolarization rate (V/s)</b>	-107.9	6.1	27	-121.7	5.9	38	<i>ns</i>
<b>Onset latency at rheobase (ms)</b>	181.2	24.3	27	139.4	17.6	38	<i>ns</i>



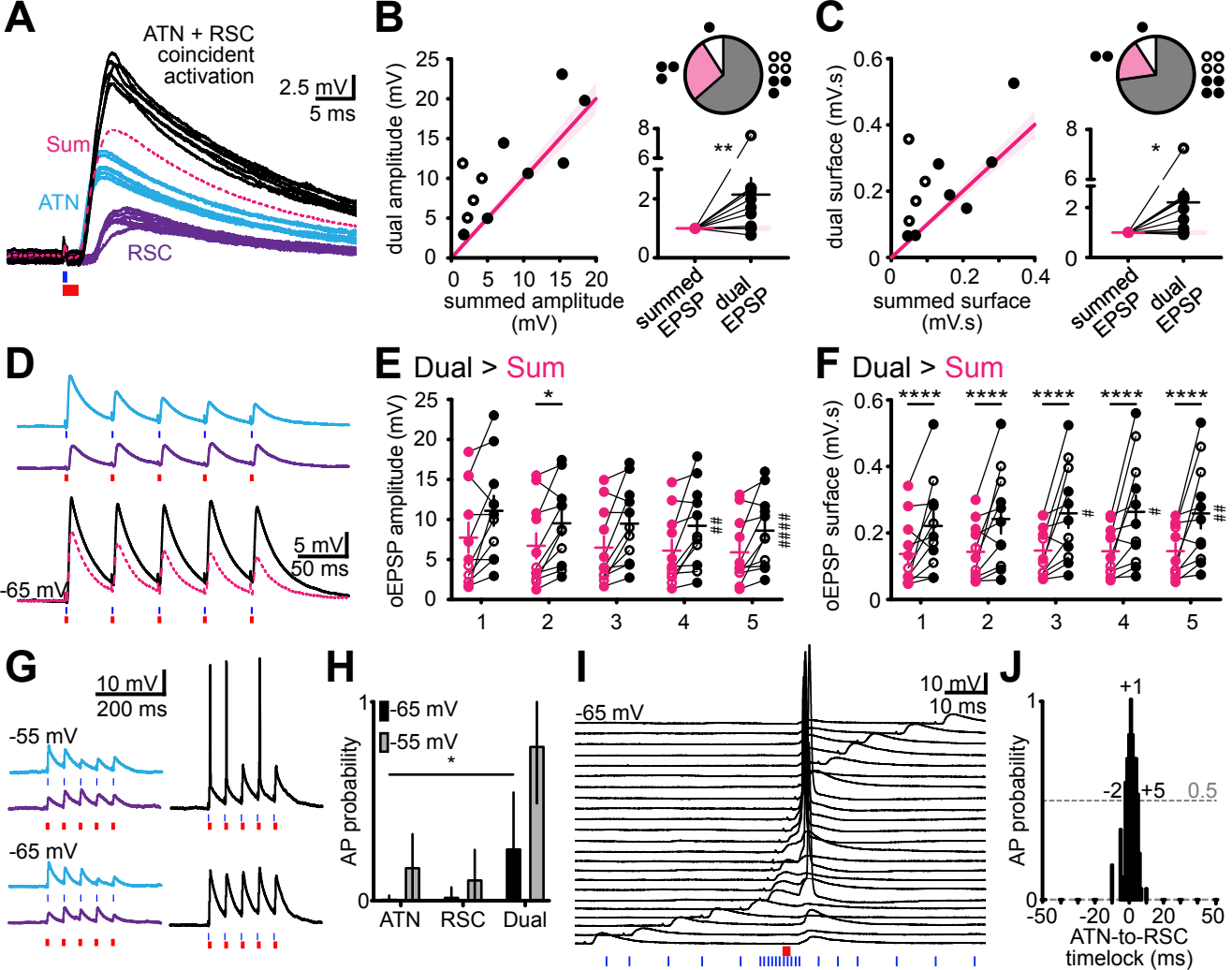






**K**

		Stim 1		Stim 2		n	Wilcoxon test
		Mean amplitude (pA)	SEM	Mean amplitude (pA)	SEM		
Chronos in ATN	Blue - Blue	-233.8	62.7	-212.1	53.3	6	ns
	Blue - Red	-220.1	46.7	-7.0	0.7	6	0.0312
	Red - Red	-9.5	3.2	-8.2	1.7	6	ns
	Red - Blue	-6.8	0.4	-194.4	40.1	6	0.0312
Chrimson in RSC	Blue - Blue	-4.1	0.3	-4.4	0.5	8	ns
	Blue - Red	-3.7	0.6	-75.3	33.8	8	0.0156
	Red - Red	-65.1	26.2	-84.0	32.0	8	0.0234
	Red - Blue	-76.7	31.4	-6.6	1.0	8	0.0078





**A**

CsGluc/QX-314

ATN

-65 mV

10 mV

200 ms

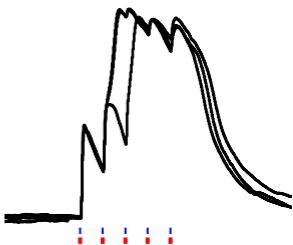
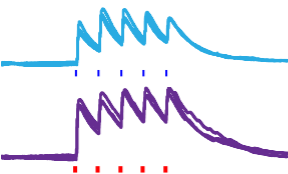
RSC

-65 mV

-65 mV

**B**

+ Gabazine

**C**

+ Gabazine + APV

